A Mössbauer Spectroscopy Investigation of Fe enriched WC-Co

Adeleke Wasiu Sufianu

A dissertation submitted to the Faculty of Science, University of the Witwatersrand, Johannesburg, in fulfillment of the academic requirements for the Degree of Master of Science.

May, 2016

DECLARATION

I, Adeleke Wasiu Sufianu, declare that this dissertation is my own work, and it is being submitted for the degree of Master of Science in the University of the Witwatersrand. It has not been submitted before for any degree or diploma examination in any other tertiary institution.

The measurements described in this dissertation were carried out at the Schools of Physics, Chemical and Metallurgical Engineering and Chemistry, University of Witwatersrand, and at Pilot Tools (Pty) Ltd.

The data analysis and interpretation is my own original work, which was carried out under the supervision of Professor Deena Naidoo (supervisor) and Dr. Hilary Masenda (co-supervisor).

The work of other scientists is duly acknowledged when used in this dissertation.

Adeleke Wasiu Sufianu

ABSTRACT

Tungsten carbide cobalt (WC-Co) cemented carbides are widely used for cutting, drilling, machining and as wear resistant materials due to the combination of high hardness and fracture toughness. In this work, we report on as-milled and as-sintered WC-10Co-20Fe samples which were ball milled for 15 hrs and sintered using liquid phase sintering (LPS). These samples were investigated by Vickers hardness test, microstructural analysis, X-ray diffraction (XRD), transmission Mössbauer spectroscopy (TMS) and conversion electron Mössbauer spectroscopy (CEMS) techniques.

A mean hardness value of 1160 ± 42 HV was obtained for WC-10Co sample while a value of 776 ± 35 HV was determined for the WC-10Co-20Fe using the Vickers hardness tester. The lower hardness value for WC-10Co-20Fe is attributed to the high volume of the binders (10% Co and 20 %Fe) incorporated in the sample. The microstructural analysis of the as-sintered WC-10Co and WC-10Co-20Fe samples reveals that the light regions represent the WC phases and the dark regions signify the presence of the Co and CoFe phases in the as-sintered WC-10Co and WC-10Co-20Fe samples, respectively. The energy dispersive spectroscopy (EDS) of the as-sintered samples shows the presence of the starting powders used (WC, Co and Fe) and some Cr contamination resulting from either the production process or the starting powders.

The resultant XRD patterns identified the WC and Co phases in the as-milled WC-10Co-20Fe sample and the WC and CoFe phases in the as-sintered WC-10Co-20Fe sample. The results obtained from the Rietveld analysis on the as-milled powder and the as-sintered WC-10Co samples shows no significant difference. For the WC-10Co and WC-10Co-20Fe samples, the WC phases seems to have little or no strain while the Co and CoFe phases have some associated strain.

Transmission Mössbauer spectroscopy studies on the milled WC-10Co-20Fe sample confirms the presence of α-Fe in the sample which suggests that no phase

transformation occurred during the milling of the starting powders. Magnetic features are evident from the conversion electron Mössbauer spectroscopy measurement on the as-sintered WC-10Co-20Fe sample. The CEM spectrum was fitted with two magnetic sextets: S1 with a magnetic splitting, B_{hf} = 34.6 T which is attributed to a phase which contains more Co atoms and not a pure α-Fe. The spectral component S2 is characterized with B_{hf} = 35.06 T and is ascribed to a disordered FeCo phase in the as-sintered WC-10Co-20Fe sample.

In conclusion, the results obtained from the different measurements will be compared and collaborated with literature.

To God
My Source, Strength and Sufficiency

ACKNOWLEDGMENTS

I would like to acknowledge the contribution and impact of people who have greatly contributed to my studies. I am greatly indebted to my supervisor, Professor Deena Naidoo for his mentorship and leadership in supervising of this research work since its inception. Thank you so much for your availability, constructive criticism, several hours of consultations despite your busy schedule and taking time out to read through the drafts of this dissertation and providing the necessary suggestions and direction.

I wish to express my sincere thanks to my co-supervisor Dr. Hilary Masenda for his assistance whom I have always seek refuge in his wealth of experience throughout my study period. A special thanks to Dr. Iyabo Usman, Dr. Philip Oladijo and his wife, Elizabeth Oladijo and Mr Kehinde Ogunyanda for being the instrument of this rare opportunity.

A special thanks to friends and colleagues: Sav Mosse, Mehluli Ncube, Nkosiphile Bhebhe, Wilfred Mbiombi, Peter Egbele, Ross Mclntosh and all students and staff in the School of Physics who have contributed one way or the other towards my studies. I am also grateful to the following people Dr. Rodney Genga for his assistance during the samples synthesis, milling and sintering, Gerrard Peters, Ndivhuwo Bryner Nelwalani for his assistance during SEM/EDS measurements, Dr. Stuart Miller, Dr. Robert Warmbier and Pilot Tools (Pty) Ltd.

I am indeed grateful to the Department of Science and Technology (DST)/National Research Foundation (NRF) Centre of Excellence in Strong Materials (CoE-SM) for financial support.

My profound gratitude goes to Bishop Michael Ayeola Okpara, a great mentor and destiny helper. My sincere gratitude goes to my parents Mr and Mrs Sufianu and all my siblings: Lekan, Kazeem, Esther and Yomi for all their prayers and support since the inception of this program. I would also like to express my gratitude to members of the Deeper Life Campus fellowship at WITS University.

Finally, I am forever grateful to God Almighty for His divine input upon my journey thus far in life. It could have not been possible without Him, to Him I am eternally grateful.

TABLE OF CONTENTS

LIST OF FIGURES

LIST OF TABLES

CHAPTER 1

INTRODUCTION

Cemented carbides are hardmetals with outstanding mechanical, physical and chemical properties which make them useful for metal cutting, mining, metal production, machining, wear parts and other industrial applications. The most commonly used hardmetals consist of tungsten carbide (WC) inside a cobalt (Co) matrix, where the hard phase is WC which promotes wear resistance while the binder phase is Co which adds ductility to the material. Cemented carbides have good wear resistance which makes them useful in many industrial applications compared to other metallurgy products. The microstructure of WC powders depends on their mechanical properties before sintering tungsten carbide cobalt (WC-Co) hardmetals [1]. In the beginning of the 20th century, cemented carbides have been commonly useful in many production processes that derived great financial profit from the combination of their fracture toughness (degree of the maximum energy a material can retain before it get to its fracture point), high hardness (the mechanical property of a material to resist plastic deformation), transverse rupture strength (ductile test to determine the strength of a material), and wear resistance. Tungsten carbide cobalt are the most viable grade of cemented carbides however due to the comparatively high price of cobalt, several efforts have been made to develop alternate hardmetals with binders such as nickel, iron, intermetallics and stainless steel which will aid the improvement of the properties of WC based materials [2, 3].

A good insight into the phase diagram of these cemented carbides is vital to predict potential phases that could be formed after sintering. The binder and cobalt phases are the characteristic phase equilibria present in cemented carbides [4]. Tungsten and carbon combine to form hexagonally closed packed (hcp) carbides which are mono tungsten carbide (WC) and bi-tungsten carbide (W_2C) as depicted by the phase diagram in Figure 1.1.

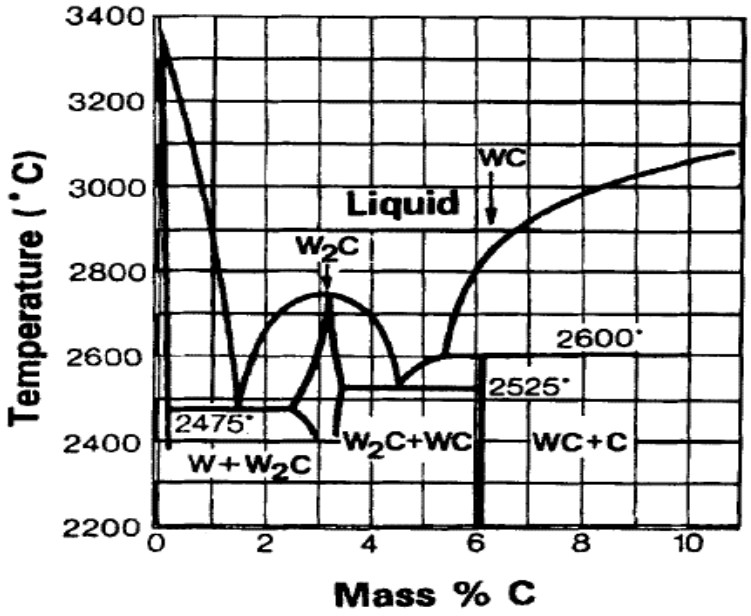

Figure 1.1: Phase diagram for the binary W-C system [5].

Figure 1.1 illustrates the different allotropic forms of the W_2C phase. The tungsten carbide system depicted above has 6.1 wt% C with a micro-hardness value of approximately 2400 kg/mm^2 , W_2C contains 3.2% of carbon with a micro-hardness value of approximately 3000 kg/mm^2 [5]. Among the most widely used metal carbides, molybdenum carbide (Mo_2C) and WC have an hcp crystal structure, while other metal carbides such as vanadium carbide (VC) and titanium carbide (TiC) are face-centred cubic (fcc). The ability of WC to wet most binder metal is better than other carbides, this property coupled with its toughness makes it the most extensively employed carbide for sintered hard materials.

Cobalt is a ferromagnetic metal with hcp structure which is stable at room temperature and experiences a change from hcp to fcc below 450^{o}C. Approximately 90% of studies on WC-hard metals employ Co as an ideal binder due to its ability to wet WC, its excellent comminution, great solubility of WC in Co during sintering and some other outstanding mechanical properties for example high hardness and toughness [4].

1.1 Background on Cemented Carbides

In 1893, Moissan [6] discovered WC in his attempt to make an artificial diamonds. During the last few decades, several attempts have been made to improve the toughness of WC. In 1920, Schröter [6] utilized Co as a binder and made a significant contribution to cemented carbides. Schröter designed the compacting and sintering procedure which are still relevant to produce WC-Co composites. Recent advancement to the alterations of Schröter's process involves replacing all or part of the hard phase with some other carbides.

1.1.1 Mechanical and Physical Properties

WC-Co hardmetals have unique properties such as high temperature strength, high hardness, outstanding fracture resistance and wear resistance. The modification of the grain size of WC and the composition of the Co binder can lead to an improvement in the properties of cemented carbides. The mechanical properties of these hard metals are usually influenced by the microstructure of the WC powders. Its physical properties depend on microstructural features like volume fraction, grain shape, particle size distributions, and the grain size of the carbide phase. The toughness, fracture strength and hardness of WC-Co ranges from about 850 to 2000 kg/mm^2 (Vickers hardness, HV), 11 to 25 MPa (fracture toughness) and 1.5 to 4 GPa (transverse rupture strength, TRS) [3], respectively. Table 1.1 gives a summary of the mechanical properties of some sintered hard materials.

Table 1. 1: Some mechanical properties of sintered hard materials [7, 8, 9].

Sintered Materials (wt %)	Vickers Hardness (HV)	Fracture Toughness ($MPa.m^{1/2}$)
WC	2660	7.2
WC-3Ni	2240	9.1
WC-10Fe	1814	10.4
WC-10Co	1333	13.5
WC-9.6Ni-0.4Co	1180	12.5

1.1.2 Applications of Cemented Carbides

Cemented carbides are essential materials to be considered when hardness and toughness properties are needed for a variety of applications. The straight WC-Co grades are most commonly used in wear resistant applications such as in cutting and machining of materials that demand abrasion resistance. These cemented carbides (WC-Co) with exceptional combination of mechanical impart strength, abrasion resistance, compressive strength, thermal shock, high elastic modulus and corrosion resistance offers potential new applications. The tendency of carbides to oppose erosion is essential in applications such as in spray nozzles/sand blast, component slices used in the oil industry and seals in slurry pumps. The hardness, rigidity and dimensional stability of cemented carbides provide an excellent performance in fluid-handling applications such as bearings valve stems, valve seats and seal rings. In addition, cemented carbides are useful in electronics devices and also to drill holes in printed circuit boards (PCB) for computers. Among the various applications of cemented carbides are tools useful in construction and transportation industries. In this century, the improvement and development of cemented carbide cutting tools have sustained exponential increase in the manufacture of metal cutting [10].

1.2 WC-Co and WC-Co-Fe

WC-Co cemented carbides in sintered or thermally sprayed forms are extensively used because of their high hardness, high temperature strength, good wear resistance, good fracture resistance for applications requiring fretting, erosion resistance, abrasion and sliding [10]. It is commercially one of the oldest and most effective powder metallurgy products. In WC-Co hardmetals, the Co binder offers support and toughness while the hard WC form the major wear resistance constituent of this material. The properties of WC-Co such as hardness, strength and wear resistance are influenced mainly by the grain size, volume of WC and also by changing the porosity of the binder and carbide phases. In the sintered material, the grain size of WC grains tend to make contact which forms an uninterrupted "skeleton" of carbide and Co binder filling the gaps between the carbide grains [11]. The mechanical properties are often tailored industrially for specific applications by changing the particle size of WC and the Co content. The smaller the size of the grain, the greater the hardness of the material and the greater the toughness, the greater the hardness of the material [12, 13].

1.3 Literature Review

The development of WC-Co hardmetals has been broadly studied in the past few decades. The high energy ball milling [14] is a desirable method to reduce the metallic systems of a crystallite size to the nanometer scale and at the same time disperse the ^{57}Fe probe atoms by mechanical alloying [15, 16]. In an earlier work conducted by Rixecker [17] on a high purity iron using transmission Mössbauer spectroscopy. The linewidth, isomer shift and magnetic split of the Mössbauer spectrum was found to be 0.29 mm/s, δ = 0 mm/s and, B_{hf} = 10.625 T which increases to 0.335 mm/s, δ = 0.007 mm/s and B_{hf} = 10.68 T respectively after milling for 24 hrs. The Mössbauer spectrum resembled a characteristic ferromagnetic α-Fe (foil thickness of 20 μm). The increase in the resonance linewidth after milling was attributed to an increase level of strain in the iron lattice which controls the nearest distances between the iron atoms and results in the distribution of the hyperfine parameters.

In a recent perturbed γ-γ angular correlation spectroscopy (PAC) and Mössbauer spectroscopy study performed by Sinha *et al*. [18] on ball-milled iron reveals that after 32 hours of milling, energy dispersive X-ray (EDX) analysis indicated that a Cr impurity concentration of approximately 5% was present during the milling process due to the steel balls used. The hyperfine field and isomer shift values are similar to macroscopic Fe samples with B_{hf} = 29.2 T ascribed to the hyperfine field shifts of the Fe probe atoms due to Cr impurities in the first or second neighbour shells. No contamination detected in the PAC spectra on the milled Fe sample after 5 hrs and two components were fitted: (1) a small broadened magnetic field which was assigned to a defect-free site and (2) quadrupole and magnetic interactions which were assigned to the surface probe.

The hardness test results reported by In-Jin Shon *et al*. [19] on polished WC-10Ni, WC-10Fe and WC-10Co utilised a Vickers hardness tester using a load of 30 kg for 15 s. The Vickers hardness values were acquired from ten measurements and the average hardness values obtained from these materials were 1776 kg/mm^2, 1750 kg/mm^2 and 1814 kg/mm^2, respectively. This shows that the Vickers hardness are very similar for all WC hard materials. The Vickers hardness measurements carried out by Kim *et al*. [20] on the WC-15Co composite material with a load of 30 kg for 15 s revealed a value of 1992 HV_{30} (where HV represents the Vickers hardness value). This average hardness value was obtained from ten measurements taken on the polished section of the WC-15Co sample.

In order to study the morphology of WC-10Co composite powder before and after milling, Zhang *et al*. [1] performed scanning electron microscopy (SEM) and found that after milling, the particle size was reduced. A comparative microstructural analysis of WC-10Co, WC-20Co, WC-6Co, WC-12Ni-6Co and WC-6Co-6Ni was conducted by Martins *et al*. [21] using SEM. The outcomes indicated that the sintering of the WC-6Co and WC-10Co powders resulted in the evenly distribution of WC and the Co binder phases and a small island of Co was observed to be present in WC-10Co powder. These authors also performed energy dispersive x-rays (EDX) analysis of the sintered materials and showed only the presence of W, C and Co from the raw materials with no sign of contamination. Kim *et al*. [22] carried out qualitative and quantitative analysis on WC and WC-3 wt% (Ni, Co and Fe) sintered

alloys using field-emission scanning electron microscopy (FE-SEM) with EDS. The findings revealed the presence of fine grains of WC and that a dense structure formed in the sintered bodies. The WC, WC-3 wt% Fe and WC-3 wt% Ni bodies were observed to have a polygonal grain structure as compared to the WC-3 wt% Co sintered body which was found to have a round shaped grains. The EDS mapping results of the WC-3 wt% Ni sintered alloy revealed that W and C were distributed evenly but Ni was distributed around the grain boundaries. The Fe and Co particles were seen to be distributed around the grain boundaries of WC in WC-3 wt% Fe and WC-3 wt% Co sintered bodies. The EDS analysis of WC-3 wt% Co sintered sample showed the presence of the starting elements with no contamination.

Mahmoodan *et al*. [23] performed X-ray diffraction spectroscopy on WC-10Co powders prepared with different ball to powder weight ratios (BPRs). The resultant patterns revealed that the WC peaks were dominant with a reduction in the sharpness with increasing BPRs which indicated that the sizes of the grain decreased with increasing milling energy.

The process of sintering WC and Co at temperatures between 1350-1450^{o}C and cooling indicated that thermal residual stresses (TRS) are produced which resulted from the difference in the coefficients of thermal expansion of Co and WC [24]. A large number of researchers [25, 26, 27, 28], have studied the stress induced in carbide grains and within the Co phase and many of the experimental results and theoretical models showed that the TRS is tensile in Co and compressive in the WC particles [29, 30, 31, 32]. Only few studies revealed that the penetration depth of Cu K_{α} radiation in WC to be very small compared to the average grain size of WC for Cu K_{α} radiation [33, 34]. An earlier study [35] showed that the residual stress in WC-Co increased up to a maximum value between 1.0 and 1.5 GPa similar to the results obtained by Hegeman *et al*. [36] whose findings showed that the residual stress increases up to a maximum near the strength of the WC.

1.4 Aims and Objectives of Study

The aim of this research work was to investigate the effect of Fe binder in the WC-10Co sample. During milling of the WC-10Co sample, Fe is often incorporated

within the matrix at very low percentages which cannot be easily detected by Mössbauer spectroscopy. Hence a reasonable fraction of Fe (20%) was introduced intentionally to the WC-Co powders investigated in this work. The milled and sintered hardmetals of WC-10Co and WC-10Co-20Fe were produced in order to:

- Investigate the hardness of the samples using the Vickers hardness test.
- Obtain microscopic information on the sample morphology and composition using scanning electron microscopy (SEM) and energy dispersive x-rays spectroscopy (EDX), respectively.
- Identify different phases by X-ray diffraction (XRD) and strain values using Rietveld analysis.
- Determine the hyperfine parameters such as isomer shift, quadrupole and magnetic splitting by performing transmission Mössbauer spectroscopy (TMS) on the milled WC-10Co-20Fe powder and conversion electron Mössbauer spectroscopy (CEMS) on the as-sintered WC-10Co-20Fe sample.
- Determine the charge state of Fe and the corresponding different phases in the material.

1.5 Dissertation Scope and Outline

The introduction, background, applications and literature review on cemented carbides together with aims and objectives of this study are outlined in the current chapter. Chapter 2 gives an account of the theory associated with the Mössbauer Effect and a discussion of the hyperfine interaction parameters. Also included will be an overview of the underlining theory of X-Ray Diffraction. Chapter 3 focusses on the sample description, milling procedure, sample mounting, grinding and polishing and the comprehensive details of the various experimental techniques (Vickers hardness test, SEM/EDX, XRD, strain analysis, TMS and CEMS) applied in this dissertation. The results and discussions are presented in Chapter 4. The conclusions and recommendations for future work are given in Chapter 5.

CHAPTER 2

BASIC PRINCIPLES OF THE MÖSSBAUER EFFECT AND X-RAY DIFFRACTION

This chapter focuses on the underlining principles of the Mössbauer effect, hyperfine interactions and X-ray diffraction. The first part of this chapter describes the concept of recoil free fraction, spectral line shape, natural linewidth, a review of electric monopole, electric quadrupole and magnetic hyperfine interactions and the associated Mössbauer parameters (isomer shift, quadrupole and magnetic splitting respectively). The final part of the chapter gives an overview of X-ray diffraction (XRD).

2.1 Mössbauer Effect

The phenomenon of resonant absorption and emission of a γ-photon without loss or gain of energy between the excited and ground states of nuclei bound in solid is called the Mössbauer Effect [37]. This phenomenon was discovered by Rudolph L. Mössbauer in 1958 [38, 39] when investigating the resonant absorption of the 129 KeV in ^{191}Ir nucleus. This effect is useful to probe the local environment of an atoms both in crystalline or amorphous solids. Detailed information about the electric, magnetic and structural properties of an atom are derived from the Mössbauer parameters which characterize the Mössbauer spectrum as a result of the hyperfine interactions. Mössbauer Effect has been used to measure small energy changes in atoms, nuclei and crystals induced by electrical and magnetic fields [40]. An isolated nucleus in an excited state decays to the ground state by releasing a γ-ray photon with energy E_γ and the nucleus recoils with energy E_R as shown in Figure 2.1 to account for conservation of energy and momentum.

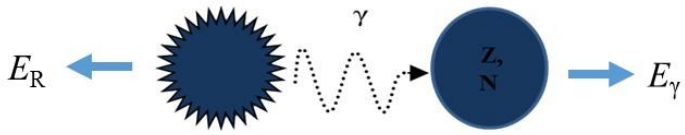

Figure 2.1: Recoil effect of the emission and absorption of gamma rays.

The energy carried by the photon, E_γ is less than the transition energy, E_o due to the recoil energy, E_R where $E_\gamma = E_o - E_R$ which prevents resonant absorption of the γ-ray. The difference in energy between the ground state and excited state is illustrated in Figure 2.2 (a) while the lack of resonance due to recoil is depicted in Figure 2.2 (b).

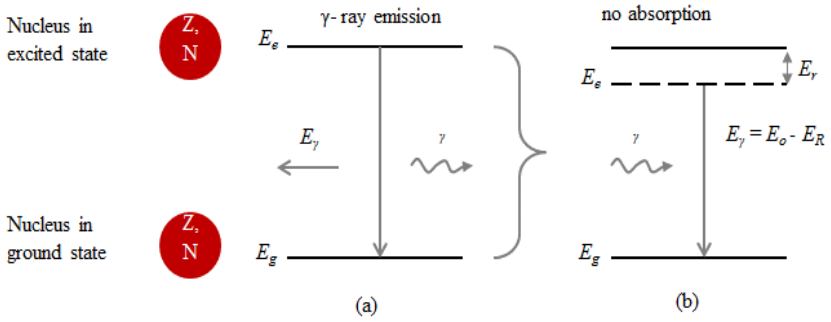

Figure 2.2: Non-resonant absorption of γ-radiation.

Conversely, when an atom (nucleus) which is bound in a crystal lattice with mass ***M***, the loss in energy due to recoil becomes infinitesimally small due to the effective mass of the whole system being much greater than the nucleus ($\boldsymbol{M} >> m$) , making E_R very small relative to E_o resulting in a nearly *recoil-free emission* of the photon. The absorption and emission of 14.4 keV γ-rays allows small energy perturbations of the order of 10^{-7} to 10^{-8} eV to be detected. Thus, this enables the determination of the atomic environment of the nuclei. When a nucleus (with N neutrons and Z protons) is in an excited state of energy E_e, a γ-photon is emitted upon decay to the ground state, E_g, as shown in Figure 2.3. De-excitation of the nucleus back to the ground state can proceed either by the emission of fluorescent photons or emission of conversion electrons.

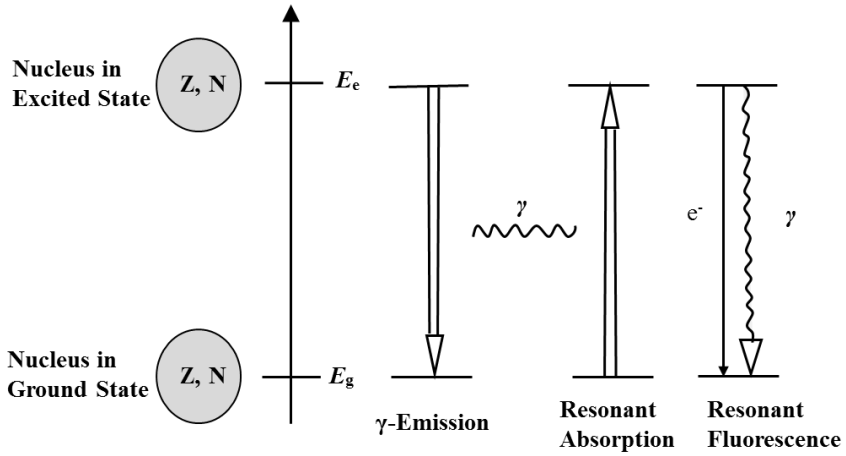

Figure 2.3: Mössbauer effect, recoilless nuclear resonance absorption and fluorescence of γ-radiation.

2.1.1 Recoil Free Fraction

The recoil free fraction *f*, is a probability of the recoilless emission and absorption of γ-rays of the Mössbauer transition which are absorbed or emitted without energy loss to nuclear recoil. It depends on the properties of the solid lattice, ambient temperature and free-atom recoil energy [41].

When a γ-ray is emitted or absorbed in a lattice, the atoms will dissipate energy through lattice vibrations as heat to the crystal. There are 3*N* (*N* is the number of atoms) vibration modes in an Einstein model each having the same frequency ω_E, such that the transfer of integral multiples of quantised phonon energy of 0, $\pm\hbar\omega_E$, $\pm 2\hbar\omega_E$,... to the lattice accompanies the emission and absorption of a γ-ray [38]. Consequently, for $E << \hbar\omega_E$, there exist a probability, of *zero-phonon transitions*, that is, transitions which take place without excitation of lattice vibrations known as the *recoil-free fraction* (f), given as

$$f = \exp\left[-k^2 \left\langle x^2 \right\rangle\right], \tag{2.1}$$

where $\left\langle x^2 \right\rangle$ is the mean square displacement of the nucleus in the x-direction. In addition, recoil free fraction *f* can be solved using Debye's model for solids as

$$f = \left\{ -\frac{3E_R}{2k_B\theta_D}\left[1+4\left(\frac{T}{\theta_D}\right)^2 \int_0^{\theta_D/T} \frac{x}{e^x-1}dx \right] \right\}, \tag{2.2}$$

where θ_D is the Debye temperature which is a measure of the rigidity of the lattice, or measures the strength of the atomic bonds in the lattice and k_B is the Boltzmann constant. The recoil free fraction is also called the Lamb-Mössbauer factor or Debye-Waller factor which can be reduced to

$$f = \exp\left[-\frac{E_r}{k_B\theta_D}\left(\frac{3}{2}+\frac{\pi^2T^2}{\theta_D{}^2}\right)\right], \qquad T << \theta_D \tag{2.3}$$

At absolute zero

$$f = \exp\left(-\frac{3E_r}{2k_B\theta_D}\right) \tag{2.4}$$

For $T > \theta_D$,

$$f = \exp\left(-\frac{6E_rT}{k_B\theta_D{}^2}\right) \tag{2.5}$$

In general, from equation (2.3), the increase in f results in a decrease in recoil energy and temperature with increasing Debye temperature depending on the material.

2.1.2 Natural Linewidth and Spectral Line Shape

The mean lifetime of the excited state is one of the most important influences on a γ-ray energy distribution. From Heisenberg's uncertainty principle, a mean lifetime (τ_N) of a nuclear level has an energy uncertainty (Γ) which is expressed as

$$\Gamma = \frac{\hbar}{\tau_N} \tag{2.6}$$

where, Γ denotes the natural linewidth, τ is the mean life, $\hbar = h/2\pi$ (h the Planck's constant). For ^{57}Fe which is the most explored Mössbauer nuclide, the energy of transition is 14.4 keV with a mean lifetime of 141 ns, 4.67×10^{-9} eV linewidth with an energy resolution of 5×10^{-9} eV which gives Mössbauer spectroscopy the highest energy resolution when compared to other spectroscopic methods [42] .

The energy distribution about E_o (transition probability which is a function of the transition energy E) can be expressed by the Breit-Wigner formula as

$$I(E) = \frac{(\Gamma/2)^2}{(E - E_o)^2 + (\Gamma/2)^2} \quad , \tag{2.7}$$

where, $\Delta E = \Gamma$ denotes the energy width with a mean lifetime (τ_N) and it gives the Full Width of the transition spectral line at Half Maximum (FWHM). Figure 2.4 depicts the Lorentzian distribution.

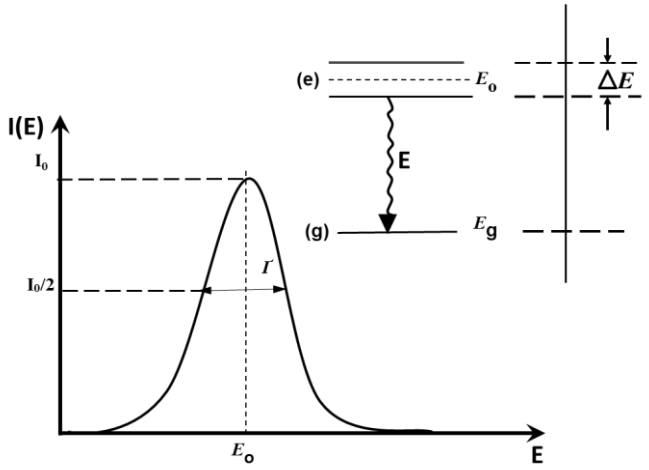

Figure 2.4: Intensity I(E) as a function of transition energy (E).

2.2 Mössbauer Spectrum

The Mössbauer spectrum is essentially a plot of the Mössbauer transition count rates as a function of the velocity of the absorber relative to the source. If there is no resonance, the spectrum will give a horizontal line with no variation; on the other hand, if there is a resonance, there will be a decrease or increase in the intensity at certain velocity values in transmission mode or backscattering mode, respectively [43] as illustrated in Figure 2.5.

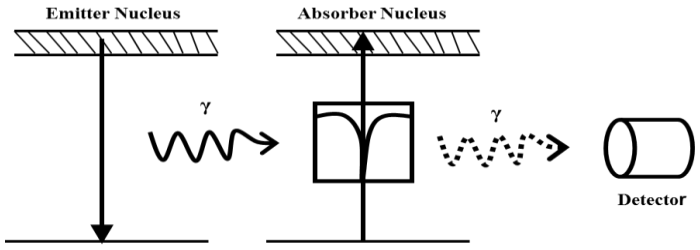

Figure 2.5: Simple Mössbauer spectrum from an identical source and absorber.

The Mössbauer parameters (the isomer shift, the electric quadrupole splitting and the magnetic dipole splitting) can be obtained from the analysis of the spectrum. A Mössbauer spectrum often demonstrates the effect of the magnetic and electric interactions between the probe atom and its surroundings.

2.3 Hyperfine interactions

The hyperfine interaction is the interaction between the nucleus and electrons which causes a very small perturbation to the nuclear energy levels when compared to the nuclear transition energy. The success of the measurement of the hyperfine interactions is the crucial reason for the utilization of Mössbauer spectroscopy in several range of applications [44]. These interactions can either split or shift the energy levels of the nucleus. The total Hamiltonian is the sum of the various contributions expressed in the form:

$$H = H_c + H_Q + H_m + H_o \tag{2.8}$$

where, H_c is the electric monopole interaction, H_Q the electric quadrupole interaction, H_m the magnetic dipole splitting and H_o represents all terms excluding the hyperfine interaction with the surrounding. Mössbauer spectroscopy can be employed to probe the hyperfine interaction for studying the microscopic environments around a nucleus. Essential information about the chemical and physical characteristics of the material understudy can be obtained from these hyperfine interactions.

2.3.1 Electric Monopole Interaction: Isomer Shift

The isomer shift is evident as shift of resonance line in the Mössbauer spectrum which results from the electric monopole interaction between the *s*-electronic charge density and the nuclear charge distribution [45]. This interaction shifts the nuclear energy levels of the absorber and the source thereby affecting the ground and excited states as illustrated in Figure 2.6.

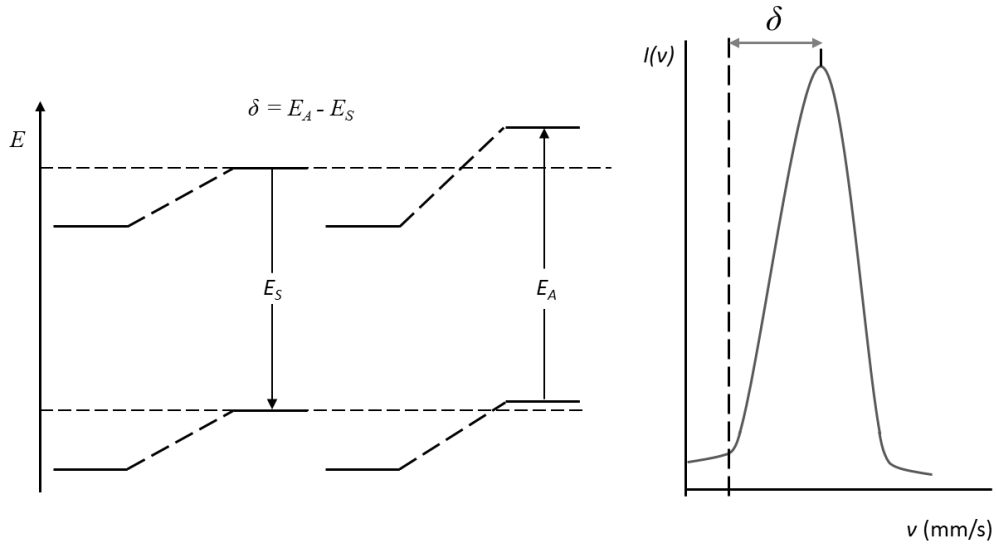

Figure 2.6: Isomer shift due to electric monopole interactions.

The energies of transition in the absorber and source are given by:

$$E_A = \frac{2}{3}\pi Ze^2 \left|\psi(0)\right|_A^2 \left[\left\langle r_e^2 \right\rangle - \left\langle r_g^2 \right\rangle\right] \ , \tag{2.9}$$

and

$$E_S = \frac{2}{3}\pi Ze^2 \left|\psi(0)\right|_S^2 \left[\left\langle r_e^2 \right\rangle - \left\langle r_g^2 \right\rangle\right] \ , \tag{2.10}$$

where $< r^2 >$ represent the expectation value of; $\left|\psi(0)\right|_A^2$ and $\left|\psi(0)\right|_S^2$ are the electron densities in the absorber and source at the Mössbauer nuclei respectively. When the absorber and source move relative to each other, there will be differences in the electrostatic shifts of the source and the absorber. This is the ***isomer shift*** given by:

$$\delta_{IS} = E_A - E_S \tag{2.11}$$

and can be written as,

$$\delta_{IS} = \frac{2\pi}{5} Ze^2 \left\{\left|\psi(0)\right|_A^2 - \left|\psi(0)\right|_S^2\right\}\left(R_e^2 - R_g^2\right) \tag{2.12}$$

where e denotes the electronic charge, R_e and R_g are the radii of the excited and ground states and Z is the atomic number. In ^{57}Fe Mössbauer spectroscopy, the isomer shift is often quoted relative to a standard reference material, with α-Fe being the most widely used. The isomer shift gives valuable information on the oxidation state, electronic spin and bonding properties such as electronegativity and

covalency. Figure 2.7 illustrates the isomer shift values of ^{57}Fe compounds for various spin and oxidation states [46].

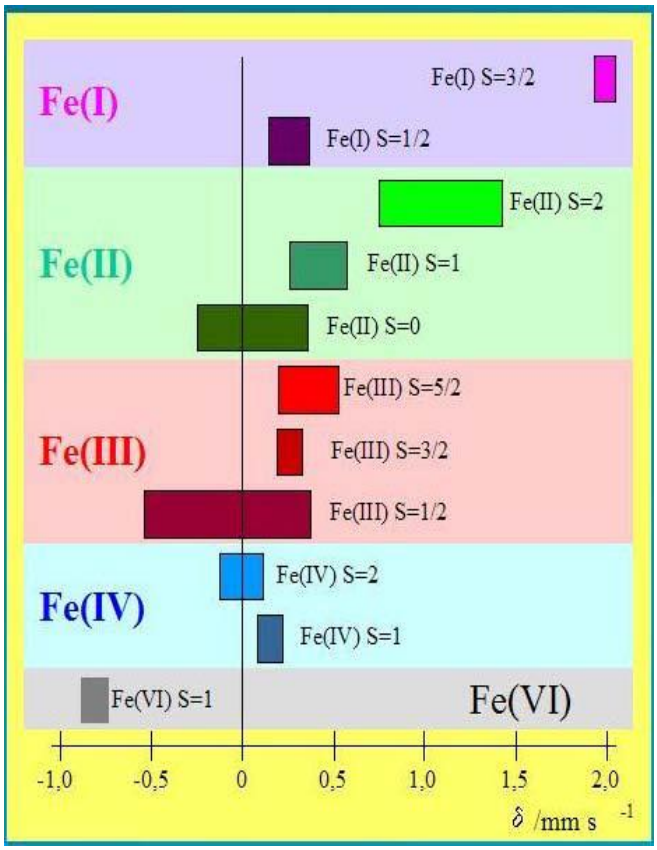

Figure 2.7: Ranges of isomer shifts observed for ^{57}Fe compounds [46].

2.3.2 Electric Quadrupole Interaction: Quadrupole Splitting

The quadrupole splitting, which arises from electric quadrupole interactions is the splitting of the energy levels produced by an inhomogeneous electric field of valence electrons and the ligands. It is determined by the principal components of the electric field gradient (EFG) tensor and nuclear quadrupole moment caused by ligands and valence electrons at the nucleus [47]. Consider a nucleus with a spin $I > 1/2$ with a non-spherical nuclear charge distribution and a non-zero electric quadrupole moment which is a (3×3) second-rank tensor and can be written as:

$$Q = \frac{1}{e}\int \rho(r)\left(3z^2 - r^2\right)dr \qquad (2.13)$$

where e is the electron and ρ the electron density. The measure of the nuclear charge distribution's deviation from spherical symmetry is nuclear quadrupole moment [48]. The electric field gradient (EFG) is a second partial derivative of the electrostatic potential and also a (3×3) second-rank tensor acting on the nucleus with elements;

$$V_{ij} = \frac{\partial^2 V}{\partial x_i \partial x_j} (i, j = x, y, z), \tag{2.14}$$

and provides insight on the location of the charge distribution relative to the crystal lattice [46, 49]. To determine the quadrupole interaction, the Hamiltonian of the electric quadrupole interaction is given by:

$$H_Q = \frac{eQV_{zz}}{4I(2I-1)}\left[3I_z^2 - I^2 + \frac{1}{2}\eta\left(I_x^2 - I_y^2\right)\right], \tag{2.15}$$

where V_{zz} denote the principal axis of the EFG, e electron charge, Q the nuclear quadrupole moment and η is an asymmetry parameter expressed as

$$\eta = \frac{V_{xx} - V_{yy}}{V_{zz}} \tag{2.16}$$

The level of the deviation from uniaxial symmetry in the presence of a uniaxial symmetry at a specific lattice site is the asymmetry parameter while the degree of electric field inhomogeneity is the electric field gradient. The EFG and nuclear quadrupole moment often splits the energy levels into sub-states with spin quantum number. The quadrupole interaction results to a splitting of a nuclear transition from a single peak into two peaks. The separation between the two peaks reflects the characteristics of the electric field at the nucleus. The distance between the two resonant lines is related to the energy difference, ΔE_Q called the quadrupole splitting and is illustrated in Figure 2.8 which is related to the bond properties and molecular structures.

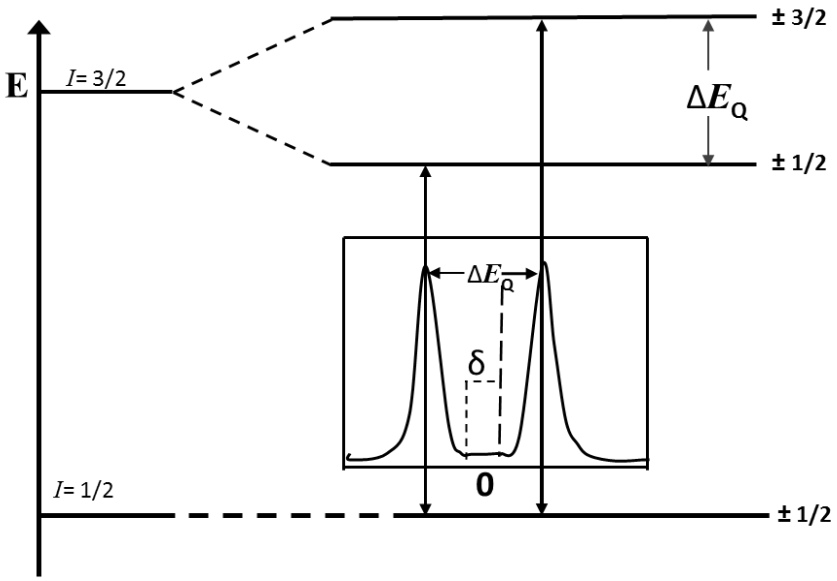

Figure 2.8: Quadrupole splitting shown by the difference in transition energy.

Thus, the quadrupole splitting reflects the local structure and symmetry of the bonding environment of a Mössbauer probe atom. The quadrupole splitting provides information such as isomerization phenomena, ligand structure, the electronic population of the different orbitals, semiconductor properties, short-lived reaction intermediates and structural defects in solids [45].

2.3.3 Magnetic Dipole Interaction: Magnetic Splitting

The magnetic splitting is due to the interaction between nuclear magnetic moment (μ) and the magnetic field (B) produced either by the neighbouring ions or electrons. The Hamiltonian for the magnetic interaction is

$$H_m = -\mu B = -g_I \mu_N I_z B \qquad (2.17)$$

where, μ is the nuclear magnetic moment, μ_N the nuclear magneton and g_I is the gyromagnetic factor of the nuclear state. In ^{57}Fe, the magnetic interaction splits the nuclear level of the nucleus with I = 3/2 into four sublevels and with I = 1/2 into (2I+1) sub-states characterized by the magnetic spin quantum number, m_I as illustrated by Figure 2.9. The selection rules for the magnetic interaction ($\Delta m_I = 0, \pm 1$) give rise to some transitions as shown in Figure 2.9 (a). This is seen as six lines in the Mössbauer spectrum commonly referred to as a sextet during the Mössbauer experiment (see Figure 2.9 (b)).

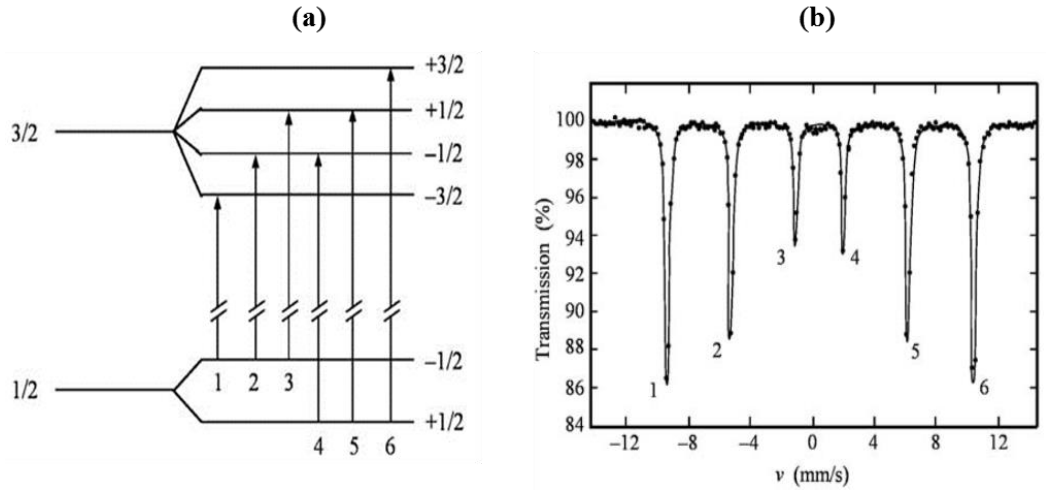

Figure 2.9: Magnetic dipole interaction resulting in the magnetic splitting of the nuclear levels [42].

The magnetic splitting gives information on the magnetic properties of the sample being investigated.

2.4 X-ray Diffraction

The discovery of X-rays has helped to probe the structure of crystals at the atomic level. X-ray diffraction is a useful technique for phase determination of a crystalline material. It can also give information on the unit cell dimensions and crystalline size of the material under investigation [50]. It depends on the dual wave/particle nature of X-rays to obtain essential information about the crystalline structure of a material.

2.4.1 Bragg's law and Diffraction

When incident rays interact with a target material, the principal effect that occurs is the scattering of the X-rays from the atoms inside the target material. These scattered X-rays often experience destructive and constructive interference which is referred to as diffraction. The diffracted waves from different atoms/planes can interfere and the subsequent intensity distribution is intensely controlled by the interaction. The array of the atoms in a periodic pattern results in the diffracted

waves having sharp peaks with regularity in accordance with the scattering of atoms.

Figure 2.10 illustrates the interaction of atoms with an incident X-ray beam.

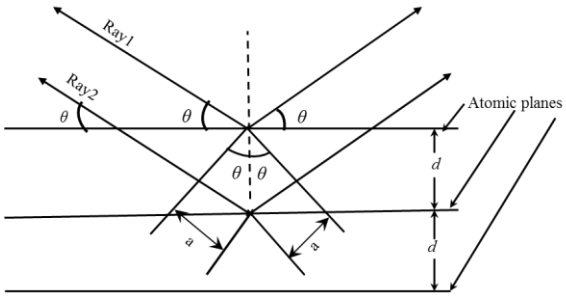

Figure 2.10: Diffraction of X-rays by a crystal.

The diffraction of X-rays by two atomic planes is governed by the path difference between the two beams. This parameter is given as $d\sin\theta$. The path difference for a constructive interference between two waves is an integral multiple of wavelengths which can be expressed as:

$$n\lambda = 2d\sin\theta \tag{2.18}$$

where n is an integer dependent on the multiplicity, θ the scattered angle, d is the interplanar spacing and λ is the wavelength. The equation above is the celebrated Bragg's law. When Bragg's law is satisfied, diffraction will occur when X-ray 1 and 2 from planes with the interplanar spacing, d [51] interfere constructively.

2.4.2 Powder X-ray Diffraction

Diffraction of X-rays is widely employed as an analytical tool for characterizing the structure of a sample. It is frequently used to investigate the physical, mechanical and chemical properties of a material. Due to its interdisciplinary nature, it is suitable for the study of superconductors and semiconductors. The sample to be investigated is usually in a powder form signifying arbitrary/random orientation of the crystalline areas in the material. The recording of a 2-D diffraction pattern indicate concentric rings of scattering peaks which correspond to the various *d*-spacing the crystal lattice [52]. To identify the principal structure of the material, the positions and the intensities are used. Figure 3.11 shows the two methods of

powder diffraction data collection viz; the transmission and reflection geometry. The particles are randomly oriented for a powder sample hence the two methods gives the same data.

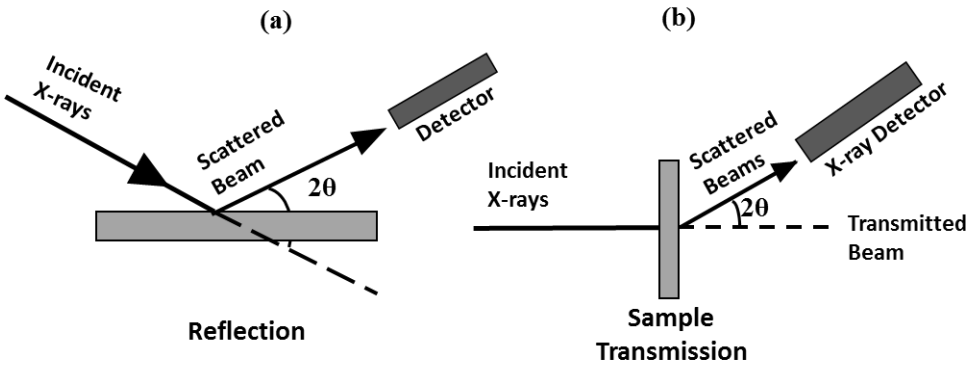

Figure 2.11: (a) Reflection and (b) transmission geometry in Powder X-ray diffraction.

CHAPTER 3

EXPERIMENTAL DETAILS

This chapter describes the different procedures used to prepare the WC-10Co and WC-10Co-20Fe samples. The first section discusses the sample specifications, milling and sintering procedures, the sample mounting, grinding and polishing processes. An overview of the various characterization techniques such as the Vickers hardness test, scanning electron microscopy (SEM), energy dispersive X-rays (EDX), X-rays diffraction (XRD), transmission Mössbauer spectroscopy (TMS) and conversion electron Mössbauer spectroscopy (CEMS) used in this work will also be presented.

3.1 Sample Description, Synthesis and Procedure

The starting materials are powder samples of tungsten carbide (WC), cobalt (Co) and iron (Fe). Table 3.1 gives the particle size of these powders. The WC is a recycled powder, Co has > 99.8 % and Fe > 99.5 % purity, respectively.

Table 3. 1: Particle size of starting powders.

Powder Samples	Particle Size (µm)
Tungsten Carbide (WC)	2-4
Cobalt (Co)	0.9
Iron (Fe)	5.0

3.1.1 Milling

The WC, Co and Fe powder samples were ball milled in a 70 mm diameter × 80 mm long stainless steel pot using a portable 100 g capacity ball mill from Pilot Tools (Pty) Ltd. A ball mill is a type of grinding mill which operates on the principle of impart and attrition and is used to grind materials into extremely fine powder. The main purpose of milling powder samples is to have homogeneous distribution of the powder samples and breakdown powder agglomerates. The WC-10Co and WC-10Co-20Fe samples were prepared as follows: 70.66 g of WC, 10.12 g of Co and 20 g of Fe were mixed together with the following

additives: 2.0 g of polyethylene glycol (PEG), 0.22 g of dispersant and 33.2 ml of pure ethanol to facilitate the reaction. Polyethylene glycol is usually used during pressing to prevent loss of compaction energy resulting from friction between the particles and the die walls. The mixtures (WC-10Co and WC-10Co-20Fe) were ball milled for 15 hrs using WC balls to powder ratio of 5:1 using a speed of 140 rpm. After milling, the milled powders were dried using a Heidolph Laborator 4010 Digital rota evaporator (School of Chemical and Metallurgical Engineering, Wits University) at 60^{o}C with a speed of 80 rpm to remove the excess ethanol. The dried powders were later sieved and pressed into green compacts.

3.1.2 Sintering

The process of applying heat or pressure to a sample without melting it to the point of liquefaction so as to form a solid mass of a material is called sintering [53]. After the milling process, the powder mixture were molded into green compacts and later sintered with a ULTAR-TEMP Sinter-HIP furnace at Pilot Tools (Pty) Ltd. The compact was then heated in vacuum (0.04 MPa) by placing it in a furnace heating chamber using an initial heating rate of 2.4^{o}C up to 270^{o}C. The fixed temperature of 270^{o}C was used for about approximately 65 minutes while the vacuum pump was switched off to enable the flow of hydrogen into the heating chamber for dewaxing (removal of waxes from the sample) to occur. Dewaxing was done in four procedures by using series of heating rates and temperature from 270^{o}C to 450^{o}C to remove the PEG. The temperature was kept constant after dewaxing at 450^{o}C for 20 minutes while the vacuum pump was turned on for the removal of hydrogen. Another heating rate of 4.2^{o}C per minute was used at a temperature ranging from about 450^{o}C to 1000^{o}C after which the maximum temperature was maintained for about 5 minutes. The vacuum pump was then turned off to permit the methane and hydrogen to flow for carbon correction. The carbon correction was performed to ensure that the carbon lost during the dewaxing was replaced [54]. The carbon control was carried out for about 90 minutes and the vacuum pump was switched on for the removal of the methane and hydrogen. Furthermore, a heating rate of 3.3^{o}C per minute was applied to increase the temperature from 1000^{o}C to 1200^{o}C. At 1200^{o}C, argon gas was added at 0.37 MPa for the cobalt loss protection (CLP). A heating

rate of 3.5 ^{o}C was carried out up to 1430^{o}C and the temperature was fixed for 75 minutes, thereafter, a hot isostatic pressing (HIP) was carried out at 4.4 MPa for approximately 20 minutes to remove surface porosity [54]. Water was then used to cool the furnace at a rate of 3.5^{o}C per minute. The sintered samples were later cut into the desired shapes for the different measurements performed within the scope of this study. Figure 3.1 illustrates the typical cylindrical shaped sample (only top view shown) after sintering.

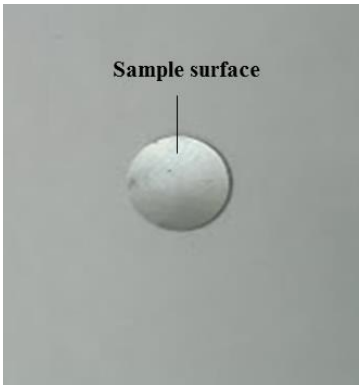

Figure 3.1: Shape of sample after sintering.

3.1.3 Sample Mounting

The sintered samples were then mounted using Opal 410 mounting Press (School of Chemical and Metallurgical Engineering, Wits University). The sample mounting was necessary to enclose the solid disk shaped samples for easy handling during grinding and polishing. Figure 3.2 shows the instrument used for the mounting of the samples.

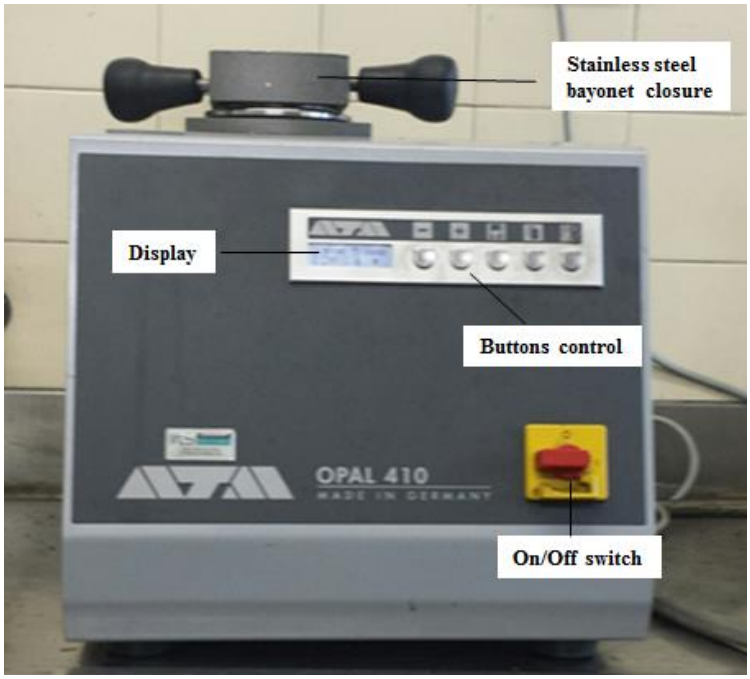

Figure 3.2: A photograph showing the Opal 410 mounting Press.

3.1.4 Sample Grinding and Polishing

The sintered samples (WC-10Co and WC-10Co-20Fe) were polished to 1 μm finished which is required for characterisation. A Struers LaboPol-5 machine was used for grinding and polishing with an applied load of 10 N for 4 s. Aka-Piatto 220 and Aka-Piatto 1200 wheels were used in the grinding process. After grinding, the samples were rinsed with water and ethanol to remove loose particles on the sample surfaces. The polishing of the samples were performed using 6 μm (for removal of scratches from the grinding process) and 1 μm (to produce a smooth surface of the sample) diamond suspension. Figure 3.3 shows the instrument used for the grinding and polishing processes.

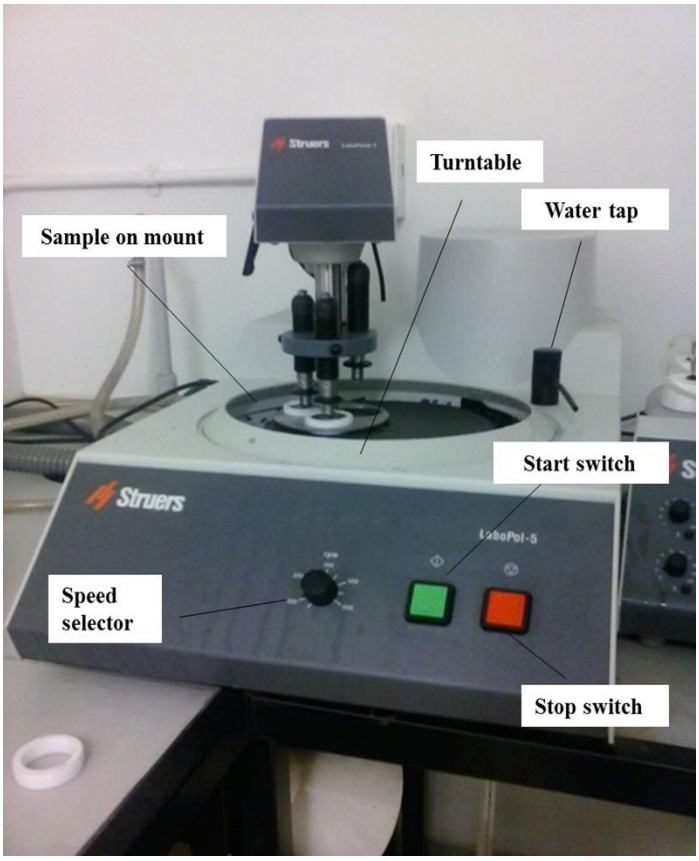

Figure 3.3: A photograph showing the Struers LaboPol-5 machine used during the grinding and polishing processes of the mounted WC-10Co and WC-10Co-20Fe samples.

3.2 Vickers Hardness Test

The Vickers hardness test is a hardness testing method developed in 1921 by R. Smith and G. Sandland [55] to observe the resistance of a material to plastic deformation. Figure 3.4 shows the Future-Tech FM-700 micro Vickers hardness tester machine used for this work.

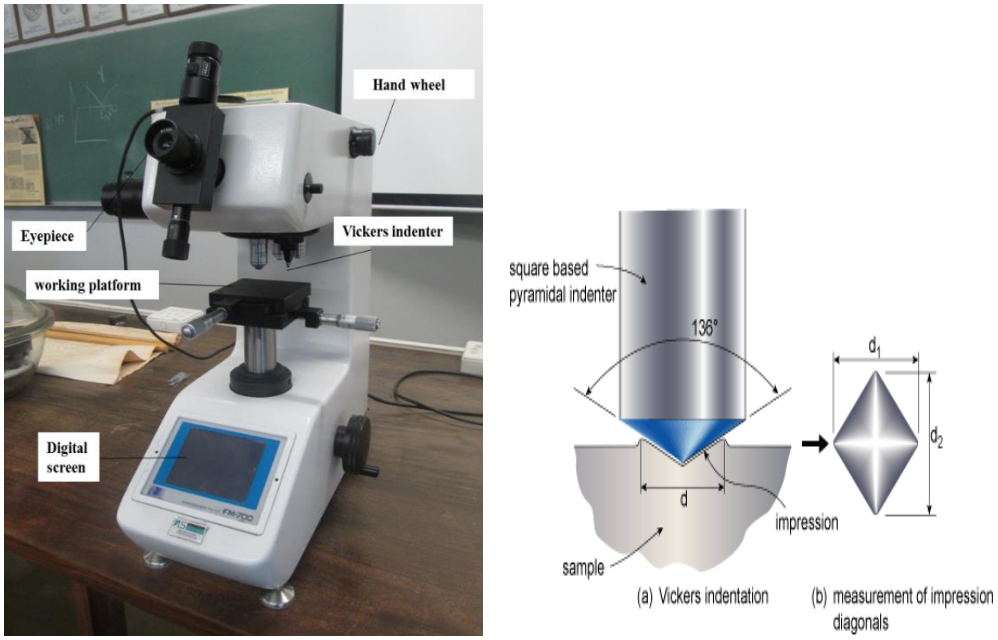

Figure 3.4: Future-Tech FM-700 micro Vickers hardness tester machine with a schematic diagram showing (a) Vickers indentation (b) measurement of impression diagonals.

A square-based diamond pyramid was employed by the Vickers hardness test as the indenter with angle faces of a pyramid of 136^{o} as depicted by Figure 3.4(a) above. The Vickers hardness is calculated by measuring the load divided by the product of the lengths of the diagonals of the square impression [56] and can be expressed as:

$$HV_{load} = \frac{F}{A} \simeq \frac{1854.4F}{d^2} \quad , \tag{3.1}$$

where, d denotes the diameter of the indenter and F the load. The Vickers hardness number for an example is usually written as: 220HV30/10 where 220 represents the hardness number, HV is the hardness scale, 30 the load applied and 10 indicates the loading time used. The Vickers hardness test is useful for all materials, has the widest scale among the hardness tests and is the most accurate measurement for hard materials [57].

3.3 Microstructure Characterisation

For the microstructure investigations of the samples understudy, scanning electron microscopy (SEM) was employed. The SEM allows for great depth of field suitable for the examination and analysis of the microstructural characteristics of solid objects. SEM utilizes intensive beam of high energy electrons to produce a range of signals at the solid surface of the sample [58]. The essential parts of the SEM are the scanning coils, electron source, electromagnetic lenses, vacuum specimen chamber and the signal detectors (secondary electron, backscattered electrons and energy dispersive X-rays). The interactions of the atoms of a sample with the intensive beam scanning electron and SEM analysis provide a wide variety of information about the sample which includes:

(a) Secondary Electron: These are electrons discharged from the atom occupying the top surface and gives the image of the surface. The sample morphology is determined by the contrast in the image [59].

(b) Backscattered Electron: These are incident electrons redirected back from a target specimen and imaged without losing much energy when the electrons of the beam collides with the nucleus of an atom. The backscattered electrons [59] depend on the atomic number and provide qualitative information for the determination of the compositional image of the sample.

(c) X-rays: During the electron bombardment, characteristic X-rays are emitted. X-rays [60] emitted from the sample can provide both the quantitative elemental information and qualitative identification about the sample.

The microstructural analysis was conducted on the polished samples using a Carl Zeiss Sigma field emission scanning electron microscopy (FESEM) with an Oxford X-act detector for energy dispersive X-ray (EDS). Zeiss SmartSEM version 5.06 interface software was used to operate the FESEM and INCA suite version 5.04 software was used to analyse the samples. Figure 3.5 shows the Carl Zeiss FESEM used for the sample analysis. Energy dispersive X-ray (EDX) was later carried out to determine the elemental composition of the binders.

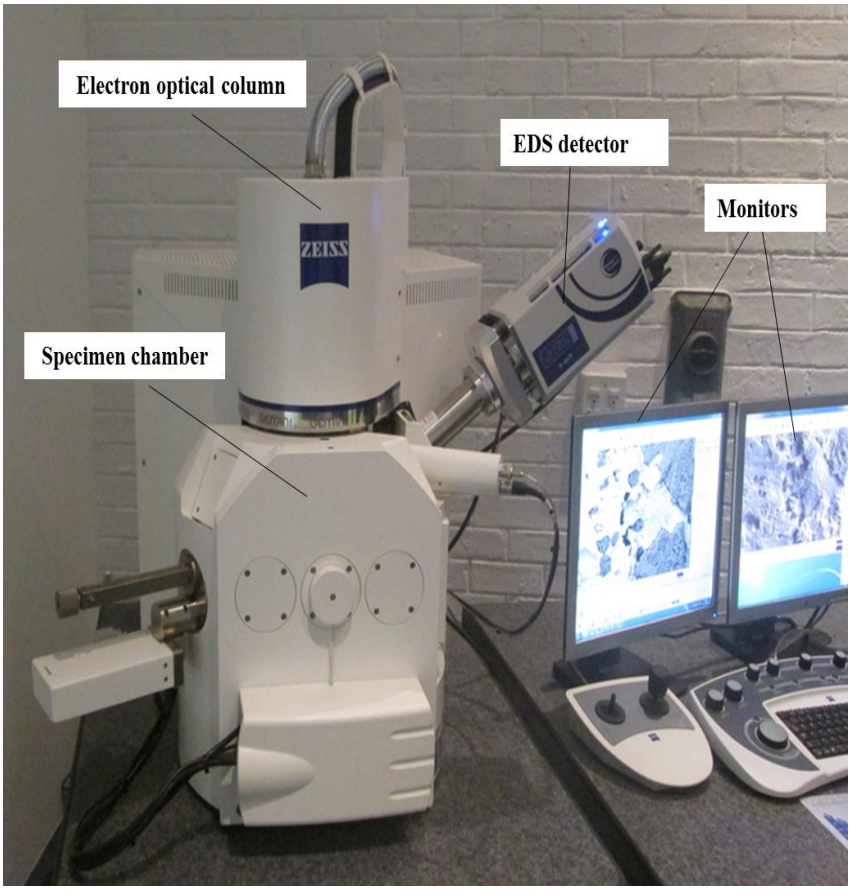

Figure 3.5: Carl Zeiss Sigma field emission scanning electron microscope.

3.4 X-ray diffraction data acquisition system

The X-ray diffraction (XRD) measurements were conducted at room temperature with a Bruker D2 Phaser desktop diffractometer (School of Chemistry, WITS University) as shown in Figure 3.6 with the insert indicating how a sample is loaded. The diffractometer was equipped with a Lynxeye detector and cobalt radiation at 10 mA and 30 kV. A 0.6 mm slit was used in operation with a 3 mm air scatter slit. The patterns were collected at a 0.026^{o} step size from $2\theta = 20^{o}$ to 100^{o} in 10 minutes intervals.

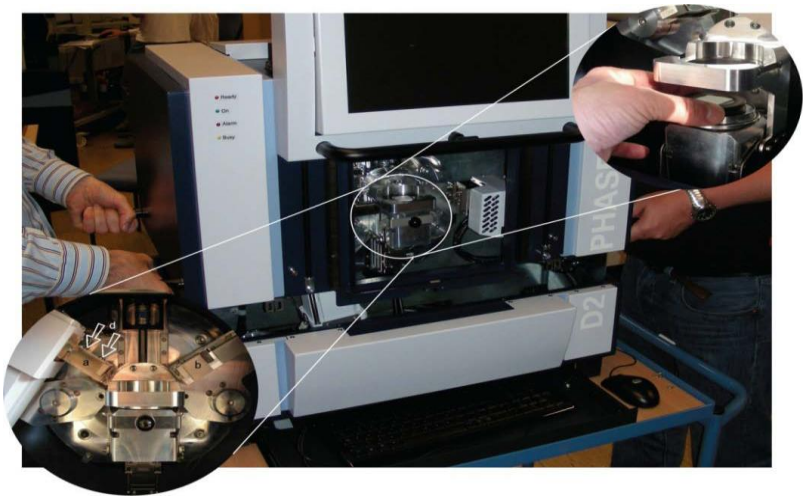

Figure 3.6: D2 Phaser desktop diffractometer, with the insert showing how the sample is loaded.

The XRD technique in conjunction with post Rietveld refinement was employed to ascertain the different phases in the samples. Strain parameters were deduced in accordance with the Topas description defined in the Topas manual (v4-2) and from research work described by Balzar *et al*. [61] .

Powder diffraction is a standard technique which is capable of providing information such as crystal structure analyses, quantitative analyses, phase identification, particle size and strain measurements. Powder diffraction is generally used in identification of unknown materials, characterization of crystalline materials, refinement of crystal structures by means of powder data, sample purity measurement and for the determination of unit cell dimensions [62]. From the XRD measurements, a Rietveld analysis was conducted to determine the residual strain in the samples under study.

3.5 Mössbauer Spectroscopy

Mössbauer spectroscopy is a distinctive technique used to investigate the electronic, magnetic and structural properties of a sample. Mössbauer spectroscopy is a non-destructive method, sensitive to the symmetry of the environments of an atom and the electron density at the nucleus. Several Mössbauer spectroscopy techniques are utilized based on the material being investigated. For this study, both the transmission Mössbauer spectroscopy (TMS) and conversion electron Mössbauer

spectroscopy (CEMS) were employed as the main investigative techniques and are discussed in detailed below.

3.5.1 Decay scheme of ^{57}Co

For ^{57}Fe Mössbauer spectroscopy, a radioactive element ^{57}Co is used as the source imbedded in a cubic non ferromagnetic material of which Rhodium is most commonly used. ^{57}Co has a half time ($T_{1/2}$ = 270 days) and decays via electron capture to the I = 5/2 excited state (136 keV) of ^{57}Fe. This state then decays to the I =3/2 excited state (14.4 keV) which in turns decays to the ground state after emitting 14.4 keV γ-ray radiation. This emitted radiation is required for Mössbauer experiment as illustrated by Figure 3.7.

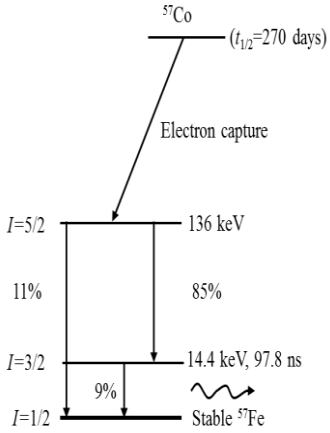

Figure 3. 7: Decay Scheme of ^{57}Co.

3.5.2 Transmission Mössbauer Spectroscopy (TMS)

A Mössbauer spectroscopy experimental set-up comprises of a γ-ray source, absorber, detector, acceleration driving devices, multichannel analyzer and a computer for spectra display and data accumulation. Figure 3.8 show a typical transmission Mössbauer spectrometer at Wits University.

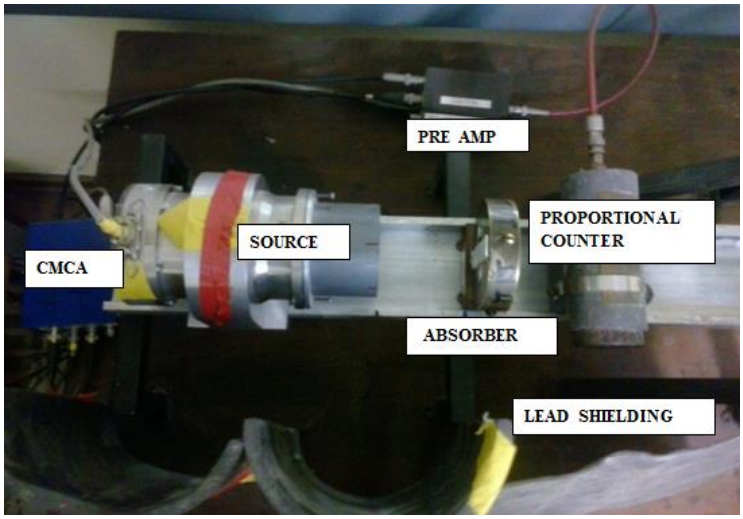

Figure 3.8: A typical transmission Mössbauer set up at Wits University.

For this layout, the distance between the source and the absorber was maintained at 10 cm and a distance of 5 cm was used between the absorber and the detector. The appropriate distances are required for the optimization of the data acquisition time which depends on the source activity, absorber characteristics and the counting performance [63] which is related to the detector characteristics such as the pulse height analyzer (PHA), dead-time, etc. For this project, a ^{57}Co (Rh) source with an activity of approximately 20 mCi was utilized and the Mössbauer spectra were collected in a horizontal transmission mode, with the velocity waveform generated by an analyzer version controller card. The spectrum was collected in 1024 channels, which was later transformed to 512 channels during the data analysis procedures.

The signals from the detector are first pre-amplified and the unipolar signals are amplified and passed through a multichannel analyzer (CMCA-550). The CMCA-550 can work in the multichannel scaling mode (MCS) window mode. For operating in MCS (Window) mode, the CMCA-550 has in additon to its digital circuit an analog circuit for data acquisition. Furthermore, analog pulses from the output of the amplifier are fed through the input analog to digital converter (ADC) on the data acquisition module to select a window for the digitalized pulses. The CMCA-550 is capable to store input pulses, filters incoming analog pulses and consequently work like a single-channel analyzer (SCA). The CMCA-550 data

acquisition module runs under Wissoft2003 [64]. The CMCA-550 module functions in two modes namely: PHA mode and multichannel scaler (MCS) mode operating in a multichannel scaling mode (MCS) where the channels are synchronized using the Mössbauer drive unit (MDU) with the aid of the feedback control system through the function generator (FG).

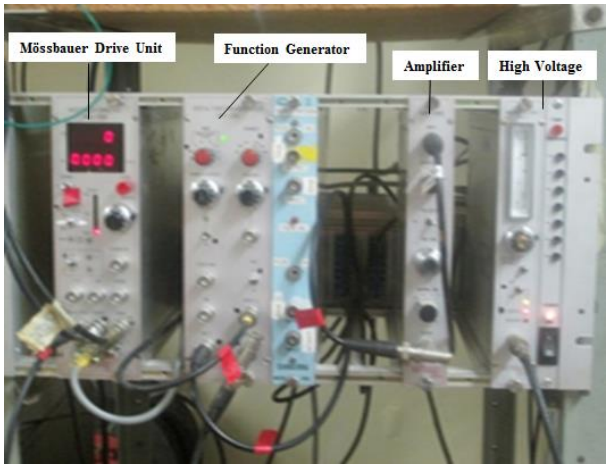

Figure 3.9: Mössbauer electronics set up at Wits University.

The FG gives a reference signal which regulates the waveform of the source. Furthermore, the FG also fives two digital control pulses (Start and Channel Advance-CHA), used to synchronize the CMCA-550. It allows to change between different data acquisition modes, start and stop data acquisition, erase, store data, display and analyse data. Figure 3.9 shows the Mössbauer electronics in operation at the Wits University. In the PHA mode, the incoming pulses are sorted into bins depending on the pulse height which is comparative to the energy of the gamma and is absorbed in the proportional counter (filled with $KrCO_2$ at about 2 atm pressure) with energy channels as shown in Figure 3.10.

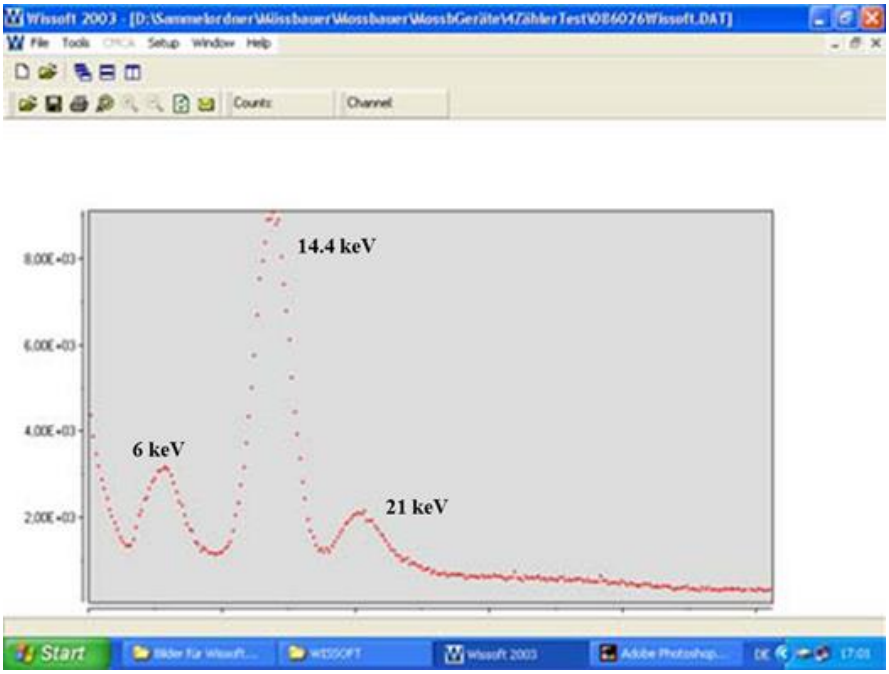

Figure 3.10: Pulse height spectrum of the ^{57}Co source.

In the MCS (Window) mode, analog pulses are fed from the output of the amplifier to the ADC of the CMCA-550 and are converted to digital counts. The ratio of the 14.4 keV γ-ray to 21 keV X-ray is first measured and later the 21 keV X-ray is removed by setting the lower level discriminator (LLD) and the upper level discriminator (ULD) windows. The 14.4 keV line of the γ-ray spectrum is then selected (see Figure 3.11) and the PHA is changed to MCS (Window) mode by using Wissoft 2003. To obtain nuclear resonance absorption, the sample to be investigated is irradiated with gamma radiation as discussed in section 3.5.1.

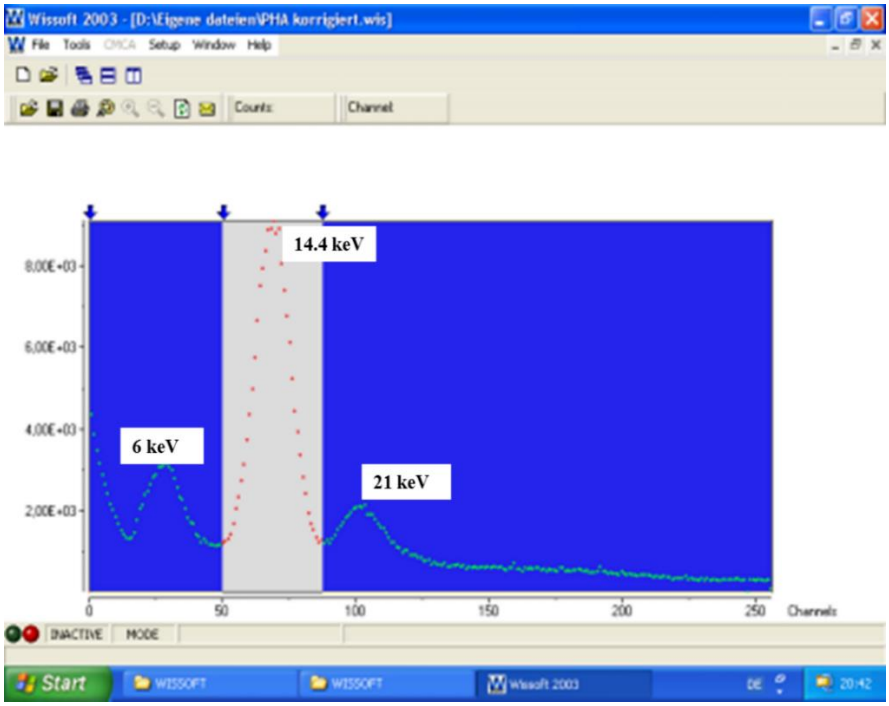

Figure 3. 11: Selection of the 14.4 keV γ-line of 57Co using Wissoft 2003.

3.5.3 Conversion electron Mössbauer Spectroscopy (CEMS)

Most of the Mössbauer spectroscopic studies are often conducted in the transmission mode which involves the detection of gamma radiation transmitted via thin absorber but when information involving the surface properties of a solid is needed, the use of transmission mode is usually limited to some absorbers. One of such possibility is the scattering technique which involves the detection of secondary radiation emitted by the absorber.

Conversion electron Mössbauer spectroscopy (CEMS) [65] can be used to investigate Mössbauer radiation in backscattering geometry. The usefulness of CEMS as a vital tool for surface analysis was first recognized by Bonchev *et al.* [66] and Swanson *et al.* [67, 68]. It is highly suitable for studying thin films and for the phase analysis of surface layers due to range of conversion of electrons with a source strength of ≈ 20 mCi. A nucleus that is promoted to an excited state by gamma ray absorption can de-excite by the emission of a gamma ray with a possibility of $N(\gamma)$, and by the internal conversion and the ejection of an electron

with the probability of $N(e)$. The internal conversion coefficient is given by $\alpha = N_e/N_\gamma$. The decay of ^{57}Fe is internally converted which results in a 91% probability of emission of a conversion electron. The internal conversion electrons consist of electrons emitted from the K, L and M shells conversions electrons with energies 7.3 KeV, 13.6 KeV and 14.3 KeV respectively. For ^{57}Fe, the K-conversion electrons have escape depth of 300 Å of the sample. The ejection of an electron creates a hole which can be occupied by an electron from an outer shell. This releases energy in the form of an Auger electron and X-ray, with the process remaining in this manner pending the dissipation of all of the energy. The principal decay scheme is depicted by Figure 3.12 below.

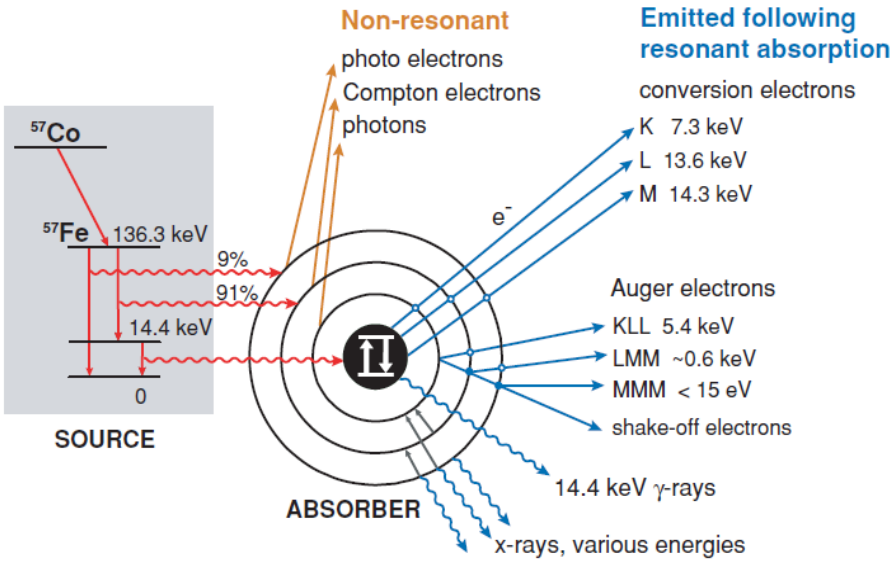

Figure 3. 12: Nuclear decay scheme of ^{57}Co to ^{57}Fe and the different backscattering processes for ^{57}Fe resulting from the resonant absorption of an incident γ-ray [39].

For CEMS, a parallel plate avalanche detector (PPAD) [69, 70, 71] has been designed where a flat plate with coated graphite is used as the anode for working in the avalanche area. In most PPADS, organic polyatomic gas is utilized as the counting gas and acetone vapour is preferably used. Parallel plate avalanche detectors are identified instruments for accurate timing measurements, no problems with radiation damage and the entire thickness of such a counter can be kept relatively thin owing to the low operating gas pressure [72]. For the CEMS measurement, the

sintered WC-10Co-20Fe sample was incorporated inside the PPAD acting as the absorber as shown in Figure 3.13 below.

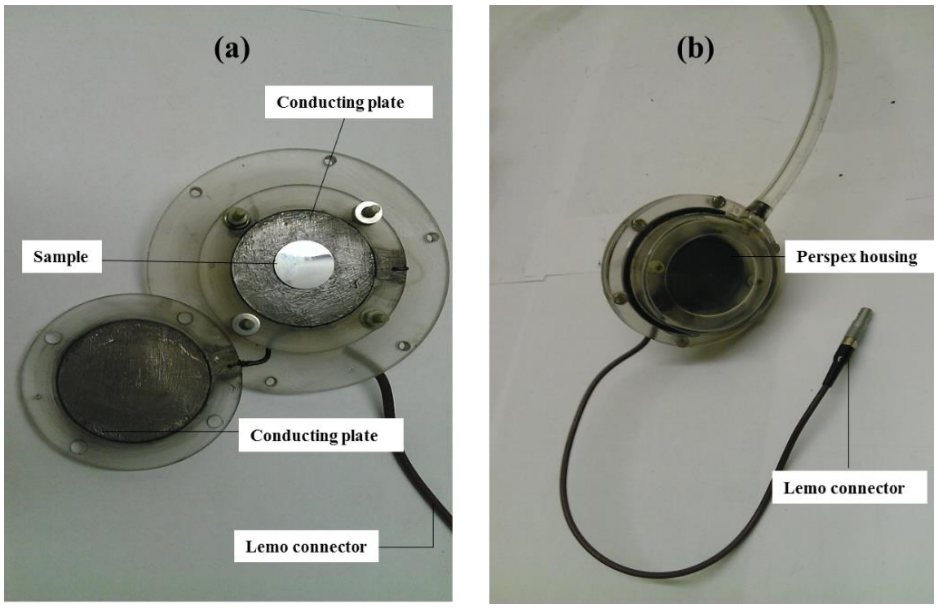

Figure 3. 13: Photograph illustrating how sintered WC-10Co-20Fe sample is inserted inside the (a) conducting plate of the PPAD and (b) sample enclosed by the perspex housing.

Inside the PPAD, there are two conducting parallel plates where a bias high voltage (~600 V) was applied to generate homogeneous electric field. The anode is connected to the ground while the sample is connected to the cathode by a graphite tape. The electric field generated by the bias voltage attracts electrons for counting purposes and the information obtained depicts the properties of the sample under study. The PPAD is then covered with Aluminum (Al) foil as shown in Figure 3.13 (a) to reduce cross section for photo-electron processes and protection from radio frequency interference. The detector is thereafter linked to a gas reservoir typically having acetone through a long thin plastic tube connected to the inlet. The set-up is then connected to vacuum pump as depicted in Figure 3.14 (b).

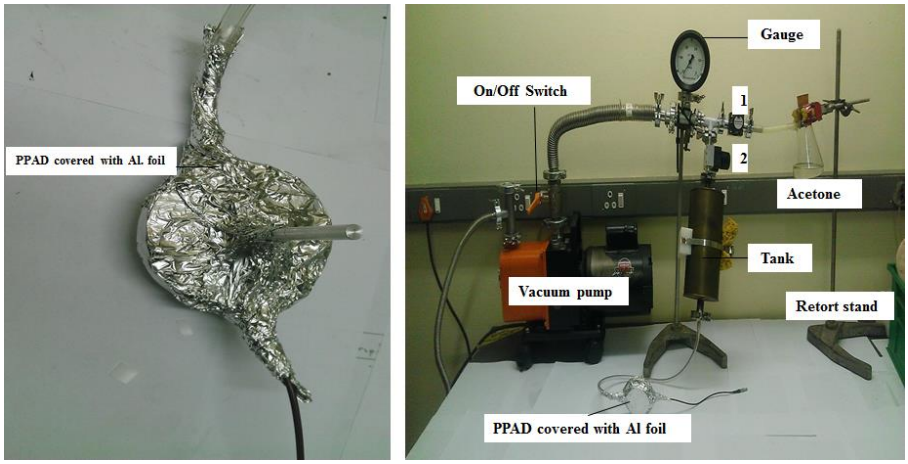

Figure 3. 14: (a) The PPAD covered with Al foil and (b) the station for pumping acetone using a vacuum system.

The acetone vapour was pumped to pressure of ~20 mbar. Thereafter the acetone filled PPAD with the mounted sample was disconnected from the pumping station and connected to the preamplifier via the lemo connector from the PPAD and a high bias voltage ranges from 500-700 V was applied. The CEMS set up used in the School of Physics, University of the Witwatersrand is shown in Figure 3.15 below.

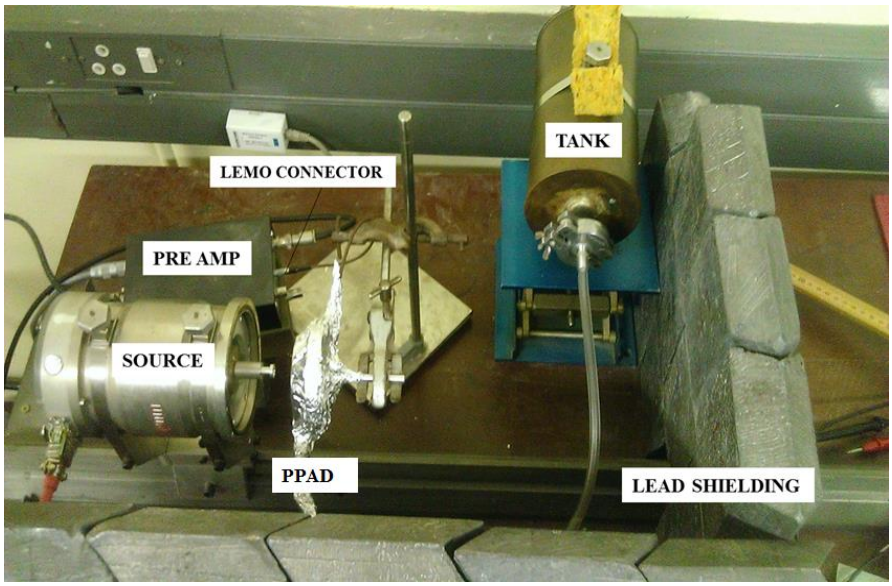

Figure 3. 15: Layout of the CEMS set up at WITS University.

3.5.4 Advantages of conversion electron Mössbauer spectroscopy

Conversion electron Mössbauer spectroscopy [73, 74] offers several advantages over other Mössbauer techniques which includes:

- The strength of CEMS is in its capacity to precisely analyse the surrounding of iron atoms in surface and subsurface regions of iron containing phases and provide vital information involving the magnetic and electronic properties of iron atom.
- CEMS is suitable to detect and identify surface phases evident in small amounts on low-area solids beyond the reach of TMS.
- This technique can be used to explore angular variations of the quadrupole doublet peak area ratios (QPAR) of specifically surface states.
- The penetration depth for the 7.3 keV K conversion electrons is below 300 nm and the energy which lost is negligible.
- The electrons are easy to be detect.
- The intensity ratio of the magnetic split peaks offers essential information on the configuration of the magnetic spin in the surface layer.

3.5.5 Disadvantages of CEMS

The CEMS technique has some limitations which include:

- The electrons progressively loose energy as they move through matter hence it is difficult to calculate their initial energy.
- The movement of the electrons through matter is not in straight lines since they collide with other electrons.
- Low counting rates and requires strong radioactive source and also enriched sample of the Mössbauer isotope.

3.6 Calibration and Analysis of Mössbauer Spectra

For this project, a program called Vinda designed by Professor Haraldur Pàll Gunnlaugsson [75] was used for the Mössbauer spectral analysis. The Vinda program is basically a toolbox which works in Microsoft Excel and all the commands are

confined in a toolbox that operates on Visual Basic Application (VBA) macros. The Vinda is an Add-In for Microsoft Excel and all the built in features of MS-Excel can be used for analysis and presentation of data. A summary of the fitting process used in Vinda is described in **Appendix B**.

^{57}Fe Mössbauer spectra are calibrated with respect to α-Fe foil. During the experiment, the spectrum is recorded twice as the source/absorber vibrates back and forth. Thus, a calibration was done to fold the spectrum and find a relationship between velocity and channel numbers which is expressed by:

$$V_i = C(i - z), \tag{3.2}$$

where, i denotes the channel numbers, C the calibration constant and z the zero velocity. The spectrum is first added and later folded using the calibration constant and the zero velocity. The spectrum of α-Fe foil as depicted by Figure 3.16 gives a six-line spectrum after folding where the centre of the spectrum was selected as zero velocity. Figure 3.16 (a) is the calibration spectra of α-Fe Foil in TMS mode while Figure 3.16 (b) depict the calibration spectra of α-Fe Foil using CEMS configuration.

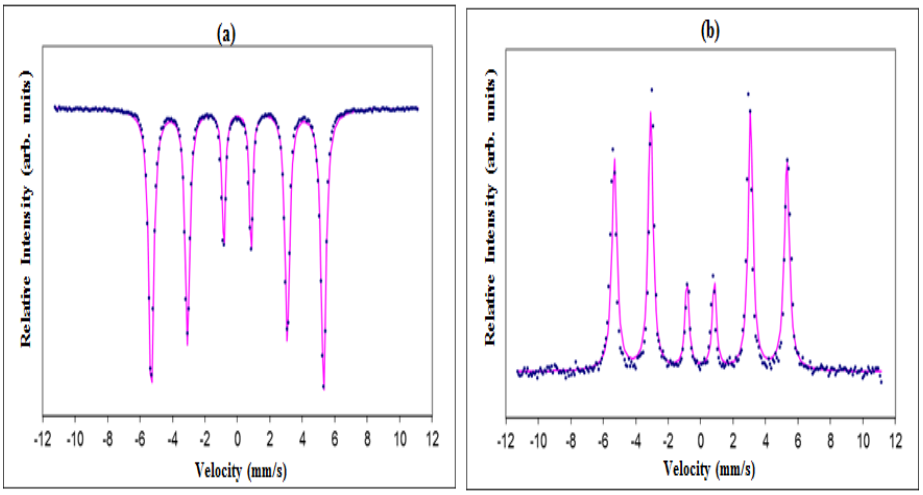

Figure 3. 16: Calibration spectra of α-Fe Foil by (a) TMS and (b) CEMS.

CHAPTER 4

DATA ANALYSIS, RESULTS AND DISCUSSION

This chapter discusses the analysis and interpretation of results obtained from different measurements undertaken in this study: Vickers hardness test, microstructural analysis, X-ray diffraction (XRD), transmission Mössbauer spectroscopy (TMS) and conversion electron Mössbauer spectroscopy (CEMS). The first section reports on the results obtained from the hardness test, microstructural analysis, XRD and strain analysis. In the last section of this chapter, the results obtained from the Mössbauer measurements on the milled and the sintered WC-10Co-20Fe samples are discussed.

4.1 Vickers Hardness Test

The hardness tests were conducted on the mounted WC-10Co and WC-10Co-20Fe samples with a Future-Tech FM-700 micro Vickers hardness tester using a load of 500 g for 15 s. Five indentation measurements were carried out at different regions on each sample and then averaged. The error values were obtained by calculating the standard deviation of the five measurements values. Table 4.1 gives a summary of the hardness test results conducted on the sintered samples. For both samples, the same starting grain size given in Table 3.1 in Chapter 3 was used. The difference in the hardness value in the Table 4.1 is due to the binder content and composition [76, 77].

Table 4. 1: Summary of the Vickers hardness results.

Sample Name	Indentation Measurements Values (HV)					Average Vickers Hardness (HV)
WC-10Co	1151	1096	1158	1207	1189	1160 ± 42
WC-10Co-20Fe	800	727	771	767	817	776 ± 35

The WC-10Co sample has a mean hardness value of about 1160 ± 42 HV while a value of ~776 ± 35 HV was obtained for the WC-10Co-20Fe sample. The decrease in hardness value is due to the increase in the binder composition. The hardness value of 1160 HV obtained for WC-10Co compares well with the value of 1100 HV

reported by Singh [78] using a load of 100 g for 5 s. The hardness value of WC-10Co-20Fe is expected since the increase in the volume of the binder results in a decrease in the hardness which is consistent with reports by Shin [79] and Ledoux *et al* [80]. These authors showed that an increase in the volume fraction of the binder carbide leads to an increase in the fracture toughness coupled with a decrease in the hardness and wear resistance of the sample. The addition of Fe-rich binders (in our case 20% volume) in the cemented carbide is expected to increase the hardness of the material as shown by Prakash [81]. In this work, the high volume of the binders (10Co and 20Fe) in the material contribute significantly to the hardness value.

4.2 Analysis of Microstructure Results

Figure 4.1 shows selected scanning electron microscopy (SEM) micrographs of (a) WC-10Co and (b) WC-10Co-20Fe sintered samples which were acquired in a scanning electron microscope using the backscattered electron mode (BSE) at different magnifications. The SEM micrographs illustrates different areas of interest, the light areas represent regions with a high atomic number while the darker areas depict regions with lower atomic number.

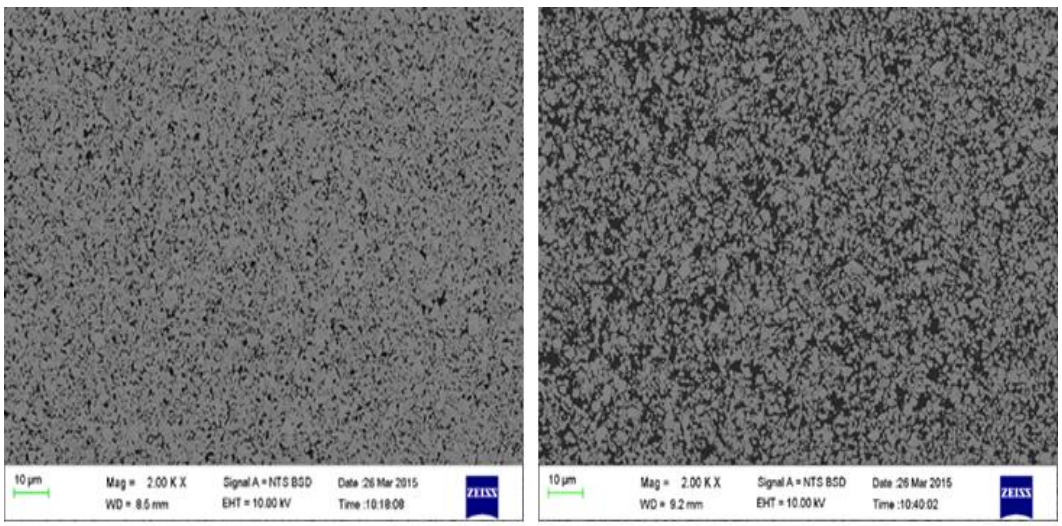

Figure 4.1: SEM micrographs of (a) WC-10Co and (b) WC-10Co-20Fe sintered samples collected in the backscattered electron mode at a magnification of 2 K.

The light areas in both samples represent the portion of the WC [82] while the dark region represent the portion of Co [21] in WC-10Co. In WC-10Co-20Fe, the Co and Fe portions are shown as dark regions. The SEM 2D scan in Figure 4.1 (a) is indicative of characteristic morphology of a sintered WC-10Co alloy sample [83]. Co is present in small islands and the distribution of the binder in the sample is fairly homogeneous except for a few enrichment zones as reported by Sun *et al*. [84]. In the microstructure of the sintered WC-10Co-20Fe sample, the distribution of WC phase in the binder is not homogeneous due to the additional binder (20% Fe) in the sample. There are some porosity observed on the sintered WC-10Co-20Fe sample which could be due to the non-distribution of the binders during milling as reported by Amberg *et al*. [85]. Figure 4.2 gives the SEM micrographs of sintered WC-10Co and WC-10Co-20Fe samples at a higher magnification of 10 K. At 10 K magnification, the majority of the WC grains have characteristic trigonal shapes with the remainder possessing multi-angular shapes. Figure 4.2 (a) shows mainly a larger WC particle size represented by the light region with irregular shapes, and few intermediate particles with less pores that represents Co shown as dark regions. No distinction could be observed between the Co and Fe binder phases in the sintered WC-10Co-20Fe sample (Figure 4.2 (b)).

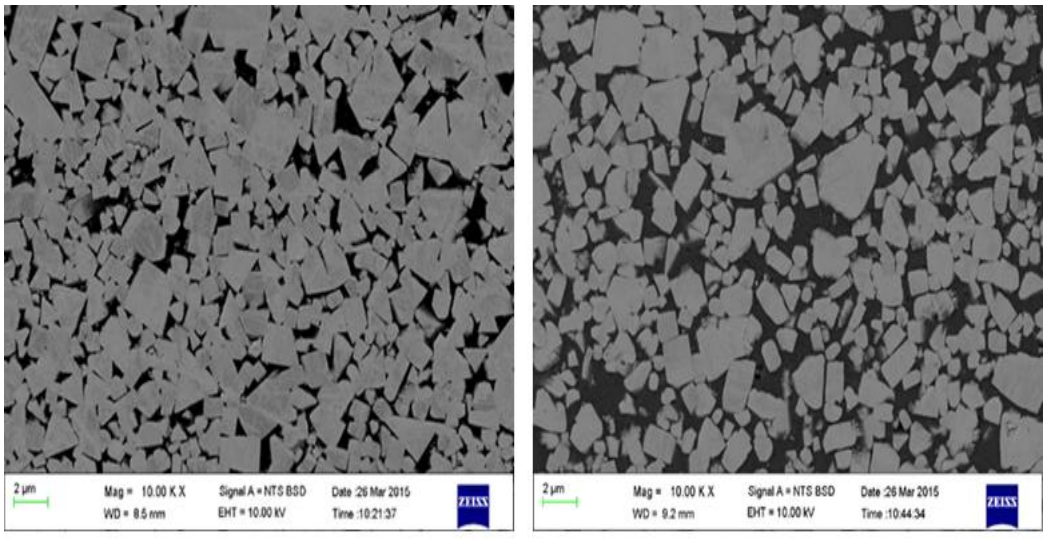

(a) (b)

Figure 4.2: SEM micrographs of (a) WC-10Co and (b) WC-10Co-20Fe samples collected in the backscattered electron mode at a magnification of 10 K.

In the sintered WC-10Co-20Fe SEM micrographs, it can be observed that when compared to Figure 4.2 (a), it can be concluded that the thickness of the binders increase inside the sample which is agreement with the result reported by Niihara *et al.* [86].

Energy dispersive X-rays measurements were performed on the sintered WC-10Co and WC-10Co-20Fe samples at an accelerating voltage of 20 kV. Figures 4.3 and 4.4 shows the spot analysis of the matrix where the energy dispersive spectroscopy (EDS) was performed and the respective EDS spectra of the elements present in the samples.

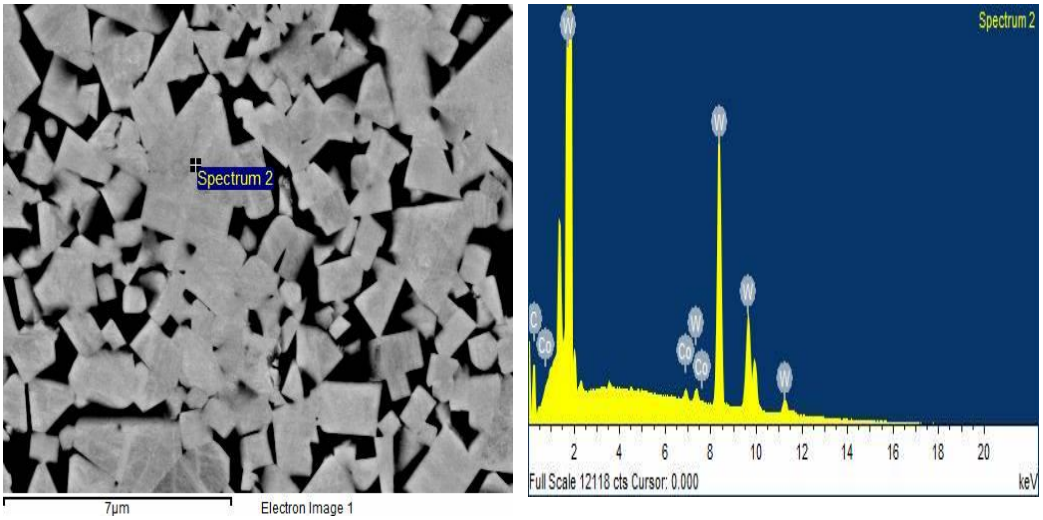

Figure 4.3: (a) EDS micrograph of the sintered WC-10Co alloy and (b) resulting EDS spectrum.

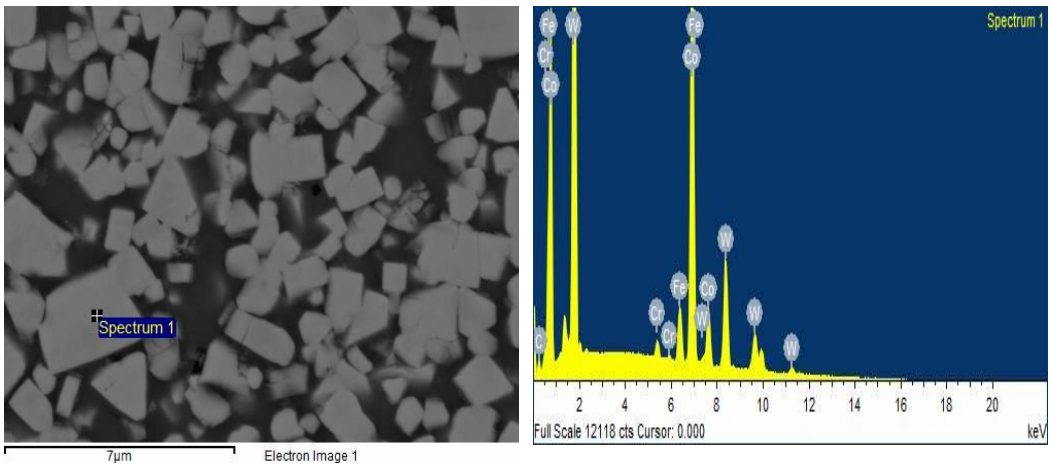

Figure 4.4: (a) EDS micrograph of the sintered WC-10Co-20Fe alloy and (b) resulting EDS spectrum.

The EDS analysis of the sintered WC-10Co alloy indicates the presence of elements from the starting powders without any impurities. The results suggests that no impurity elements were found except for constituent elements W, C and Co is similar to the findings obtained by Kim *et al*. [22]. However, the EDS analysis of the sintered WC-10Co-20Fe indicates the presence of the starting powders (W, C, Co, Fe) and Cr contamination. The wt% of Cr present is 0.21 % which is in reasonable agreement with the result reported by Suryanarayana [87] where a slightly larger fraction of 1 wt% was reported due to the powders milled in a steel medium. These contaminations reported in this study could have originated from the recycled powders used or from the production process. Some contaminations often result from the milling media, particle size of the powder and the formation of new surface during sample production [88].

4.3 X-ray diffraction results

X-ray diffraction (XRD) was conducted at room temperature on the milled WC-10Co and WC-10Co-20Fe powders and on the WC-10Co and WC-10Co-20Fe sintered samples. These measurements were performed with a Bruker D2 Phaser (generation 1) equipped with a Lynxeye detector and cobalt radiation at 30 kV and 10 mA. The XRD patterns for the as-milled and the as-sintered samples were recorded with a 0.026 θ step size from 20^{o} –100^{o} in 2θ for 10 minutes and the data was analysed using the multiphase 'fingerprint' process within the EVA software. Figure 4.5 illustrates the XRD patterns for the as-milled and as-sintered WC-10Co samples while Figure 4.6 gives the XRD patterns for the as-milled and the as-sintered WC-10Co-20Fe samples.

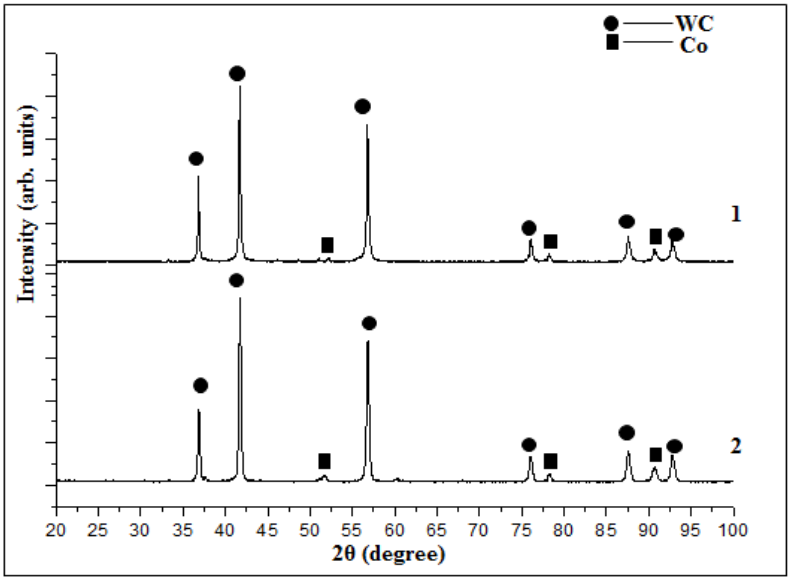

Figure 4.5: **The fingerprint of the different phases for the (1) as-milled and (2) as-sintered WC-10Co samples.**

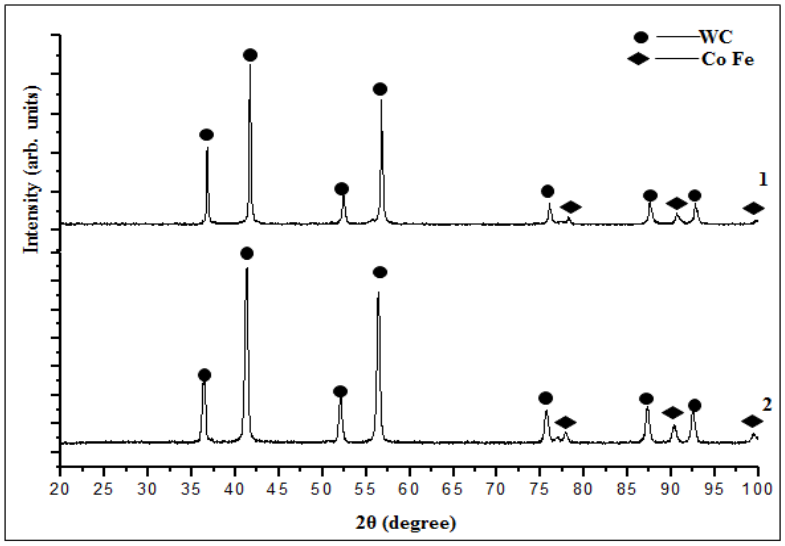

Figure 4.6: **The fingerprint of the different phases for the (1) as-milled and as-sintered WC-10Co-20Fe samples.**

The phase analysis indicates the presence of mainly the WC and Co phases in the as-milled and as-sintered WC-10Co samples while WC and CoFe phases were observed in the as-milled and as-sintered WC-10C-20Fe samples. The diffraction peaks of Co phases are slightly lower than WC. Such phases (WC and Co) have

been reported by other researchers [89, 90] for both as-milled powder and as-sintered WC-10Co samples. Here it must be noted that Co does not fluoresce with Co radiation, the elements which strongly do are Mn, Cr and V. Cu radiation causes fluorescence with Co that is why a Co target was used. The X-ray radiation emitted from Co is different to its absorption edge energy band.

4.4 Rietveld Analysis

The XRD patterns for the as-milled and as-sintered WC-10Co and WC-10Co-20Fe samples were refined using the Rietveld method [91] to determine the strain induced in the sintered samples. The as-milled powders of WC-10Co and WC-10Co-20Fe were used as the reference samples for the description of the peak shape and instrument contributions. The derived analytical values were used for the strain analysis of the as-sintered WC-10Co and WC-10Co-20Fe samples using the Rietveld refinement method in accordance with the Topas description defined in the Topas manual (v4-2) described by Balzar *et al*. [61] . The analysis gives the strain value and not the stress tensors. No spherical harmonics have been used to determine the tensors. The strain ratio determined is the change between the as-milled and as-sintered samples and may not represent an absolute value. Figures 4.7 and 4.8 depict the XRD patterns for the as-milled powder and as-sintered WC-10Co samples from which the strain was obtained using Rietveld analysis. The green and red solid lines represent the experimental and fits to the data, respectively while the black solid lines are indicative of the errors.

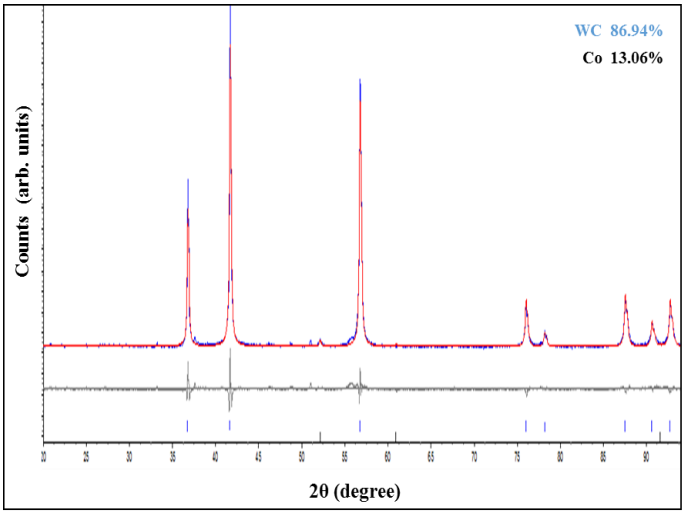

Figure 4. 7: XRD pattern for the as-milled WC-10Co powder sample.

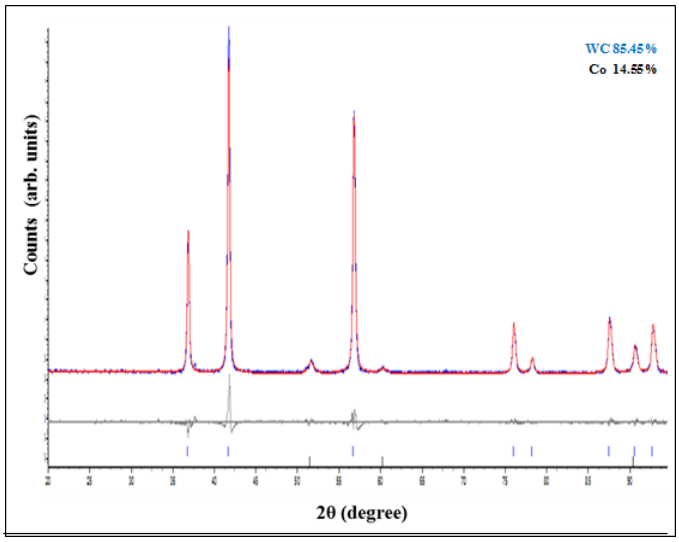

Figure 4. 8: XRD pattern for the as-sintered WC-10Co sample.

The X-ray diffraction patterns for the as-milled powder and the as-sintered WC-10Co samples showed no significant difference. The XRD pattern for the as sintered WC-10Co sample shown in Figures 4.7 and 4.8 reveals the presence of only WC and Co indicating that there was no compositional change during the sintering process which is similar to the result reported by Shon *et al.* [92]. Figures 4.9 and 4.10 illustrate the XRD patterns for the as-milled powder and as-sintered WC-10Co-20Fe samples which shows slight peak broadening resulting from the

reduction in the particle size due to milling as seen on the XRD peaks [93]. The grain size influences the broadness of diffraction peaks. However, an increase in grain size is inversely proportional to peak widths. An increase in strain is directly proportional to peak width. Therefore, any increase in broadness due to heat treatment of the material would result in strain at the domains (assuming that the effect of heat could cause an increase in domain size).

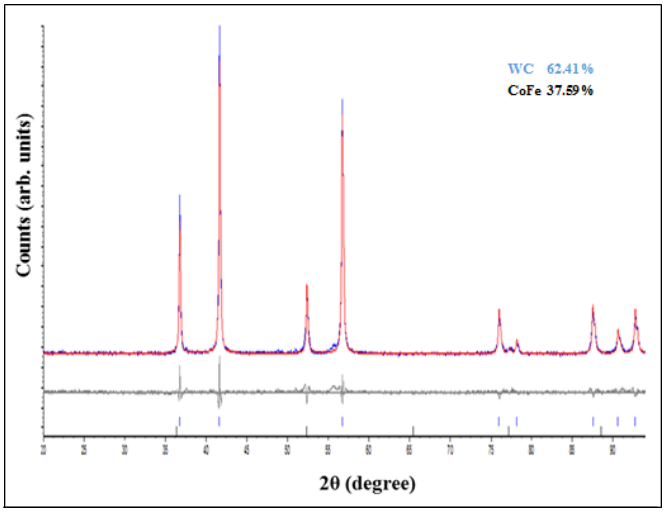

Figure 4. 9: XRD pattern for the as-milled powder WC-10Co-20Fe sample.

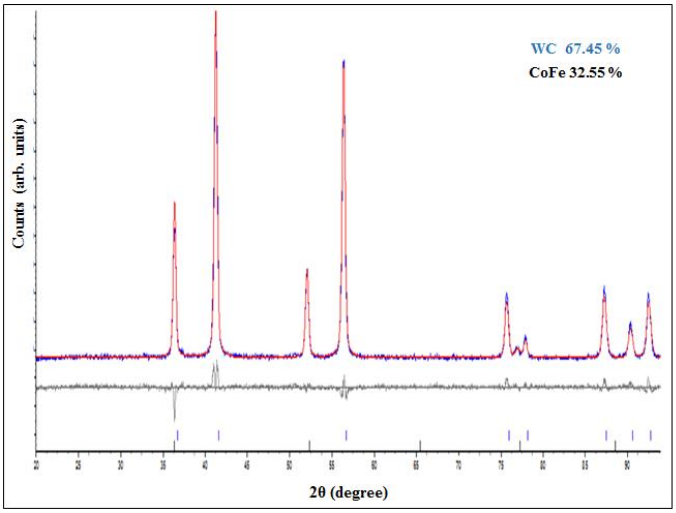

Figure 4. 10: XRD pattern for the as-sintered WC-10Co-20Fe sample.

The XRD analysis of the as-milled WC-10Co-20Fe sample indicates the presence of WC and Co phases while the XRD analysis for the as-sintered WC-10Co-20Fe sample confirms the presence of WC and CoFe phases. For the as-sintered WC-10Co sample, the 'WC strain ratio' was established as 3.62×10^{-7} and the 'Co strain ratio' was found to be 7.07×10^{-4}. The 'WC and CoFe strain ratios' for the as-sintered WC-10Co-20Fe sample was determined to be $2.18\times10^{-7}$and 1.28×10^{-3}, respectively. More details on Rietveld refinement are in Appendix A. Table 4.2 gives the summary of the results obtained using the Rietveld analysis.

Table 4. 2: Summary of the residual strain results obtained from Rietveld analysis on data acquired for the WC-10Co and WC-10Co-20Fe samples.

Sample	WC strain ratio	Co strain ratio
WC-10Co	3.62×10^{-7}	7.07×10^{-4}
WC-10Co-20Fe	2.18×10^{-7}	1.28×10^{-3}

For the as-sintered WC-10Co sample, the tungsten carbide (WC) phase appears to have little or relatively insignificant strain while the Cobalt (Co) phase however seems to have strain associated with it. In the as-sintered WC-10Co-20Fe sample, the WC phase appears to have little strain or relatively insignificant strain while the CoFe phase however appears to have strain associated with it.

4.5 Mössbauer measurements, data analysis and results

Mössbauer measurements were conducted at room temperature using two modes: transmission Mössbauer spectroscopy (TMS) on the as-milled WC-10Co-20Fe powder sample and conversion electron Mössbauer spectroscopy (CEMS) on the as-sintered WC-10Co-20Fe sample to determine the isomer shift, quadrupole and magnetic splitting. Both measurements were conducted using approximately 20 mCi ^{57}Co (Rh) source. A calibration measurement was performed in both TMS and CEMS configurations before the actual measurements for the samples under

study. The analysis of the calibration data and the obtained hyperfine parameters are discussed in subsequent sections.

4.5.1 TMS calibration spectrum

A Mössbauer calibration spectrum of α-Fe foil (thickness of 12.5 µm and 99.99% of high purity) was recorded at room temperature as shown in Figure 4.11 using the TMS mode for approximately half a day to obtain data with good statistics. The spectrum was fitted using the Lorentzian model and one sextet was obtained. The fitting routine is described in the Appendix B.

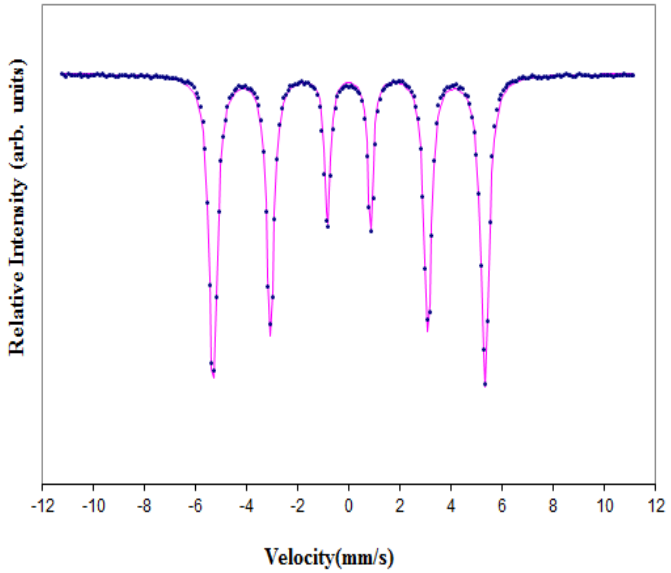

Figure 4. 11: Calibration spectrum of the α-Fe foil recorded in the TMS mode.

The fitting routine (describe in Appendix A) yielded values for the magnetic hyperfine field, B_{hf} = 32.9 T, an isomer shift δ = 0.001 mm/s and a quadrupole split, $\Delta E_Q \approx 0$ mm/s, which are typical values for α-Fe [94].

4.5.2 TMS results of milled WC-10Co-20Fe sample

A transmission ^{57}Fe Mössbauer measurement was performed on the milled powder WC-10Co-20Fe sample to ascertain the possible phases after mixing and milling. The Mössbauer spectrum for the as-milled WC-10Co-20Fe powder sample shown in Figure 4.12 was fitted with one ferromagnetic sextet denoted by S1 using the Lorentzian model.

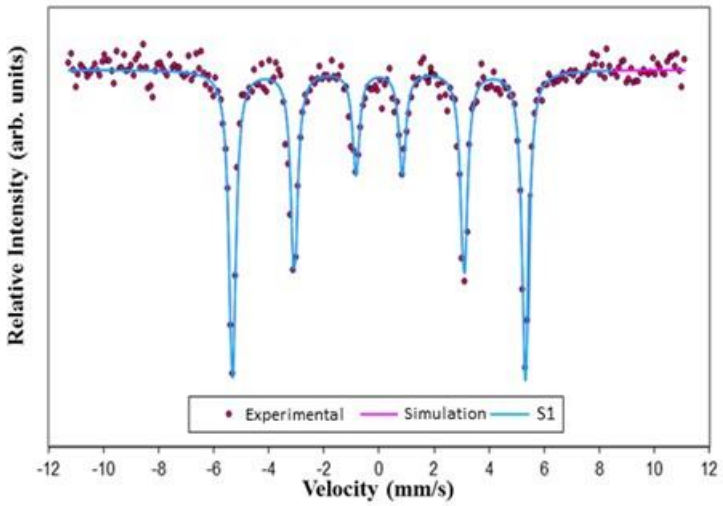

Figure 4. 12: TMS Mössbauer spectrum for the milled WC-10Co-20Fe sample.

The hyperfine parameters obtained from the fits to data for the as-milled WC-10Co-20Fe sample at room temperature are presented in Table 4.3. All reported isomer shift values are reported relative to α-Fe.

Table 4. 3: Mössbauer parameters of the milled WC-10Co-20Fe sample.

Sample	Component	δ (mm/s)	ΔE_Q (mm/s)	B_{hf} (T)	Relative Area (%)
WC-10Co-20Fe	S1	0.001(3)	-0.007(6)	32.96(2)	100

The Mössbauer spectrum obtained for the as-milled WC-10Co-20Fe sample exhibits a six- lines pattern. Sextet 1 (S1) is characterized with hyperfine parameters (see Table 4.4) similar to α-Fe. This suggests the presence of α-Fe in the sample as the only possible iron containing phase. This does not however eliminate the

possibility of new non-Fe containing compounds/phases being formed after milling. The presence of iron in the starting powders was revealed also from the SEM/EDS results as illustrated by Figure 4.4. The XRD analysis also confirms the existence of iron in the sample. The extracted hyperfine parameter values obtained from this study are consistent with results obtained by Jartych *et al.* [95] for electrodeposited iron layers. These authors determined values for B_{hf} = 32.9 T, δ = -0.01 mm/s and $\Delta E_Q \approx$ 0.0 mm/s which are consistent with those of α-Fe. A similar results was reported by Zhang [96] for α-Fe on iron compound nanocrystal samples who found hyperfine parameters corresponding to B_{hf} = 32.9 T, δ = -0.01 mm/s and $\Delta E_Q \approx$ 0.0 mm/s.

4.5.3 CEMS calibration spectrum

The CEMS calibration spectrum was conducted at room temperature on an α-Fe foil with the same specifications (thickness of 12.5 µm and 99.99% of high purity) as in the TMS measurement. The data was recorded for approximately 21 hrs to obtain a spectrum with good statistics. Figure 4.13 depicts the CEMS spectrum for α-Fe which has been fitted with one six-line pattern using the Lorentzian model by employing the minimization routine (see Appendix B) to check the goodness of fit with an ideal χ^2 = 1. The extracted hyperfine parameters were determined as B_{hf} = 32.9 T, δ = 0.001 mm/s and ΔE_Q of 0 mm/s.

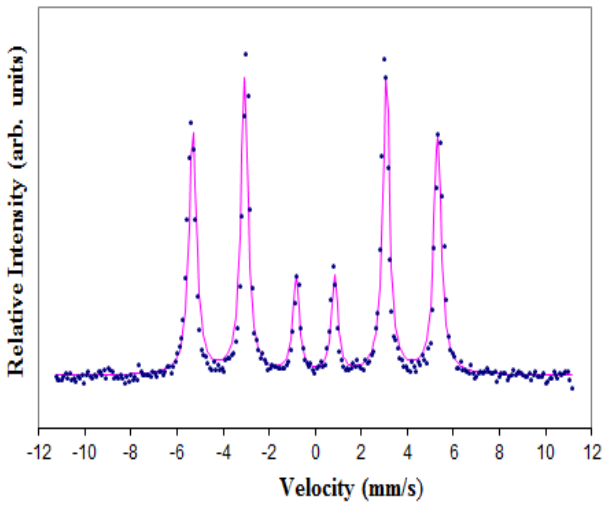

Figure 4. 13: Calibration spectrum of α-Fe from CEMS.

4.5.4 CEMS results of sintered WC-10Co-20Fe sample

The analysis and results procedure of the CEMS data collected at room temperature on the as-sintered WC-10Co-20Fe sample is presented in this section. The conversion electron Mössbauer spectrum for the as-sintered WC-10Co-20Fe sample is shown in Figure 4.14 below together with the fitted spectral components.

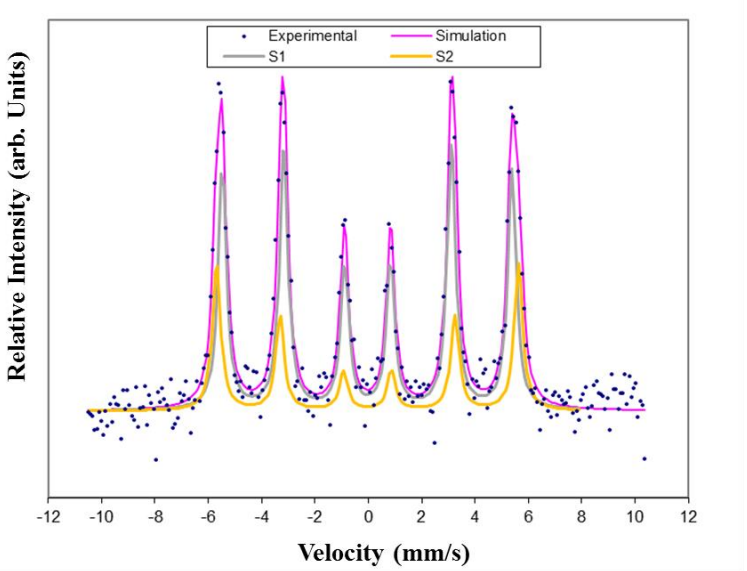

Figure 4. 14: Room temperature CEM spectrum for the sintered WC-10Co-20Fe.

The CEM spectrum was fitted with two sextets. The extracted hyperfine parameters are listed in Table 4.4. The isomer shift values are given relative to α-Fe.

Table 4. 4: Hyperfine parameters obtained for the sintered WC-10Co-20Fe sample.

Components	δ (mm/s)	ΔE_Q (mm/s)	B_{hf} (T)	Rel. Area (%)	Γ (mm/s)	Area (%)
S1	-0.036(3)	-0.018(7)	33.60(4)	70	0.38	-1.82(6)
S2	-0.033(8)	0.01(2)	35.06(7)	30	0.38	-0.79(6)

The hyperfine field of 33.60 T for S1 obtained in this study is similar to the hyperfine field of 33.9 T reported by Alcázar *et al.* [97] which is attributed to a phase which is not a pure iron but having more of Co atoms. The extracted hyperfine field of 35.06(7) T and δ = -0.036(3) mm/s for S2 is similar to the values of

B_{hf} = 34.6(2) T and δ = +0.035(5) mm/s reported by Collins *et al*. [98] for the disordered FeCo phase in the $Fe_{50}Co_{50}$ system produced through mechanical alloying. This spectral component is tentatively assigned to Fe atoms in a more Co-rich or Fe-rich local environments. The hyperfine field of 35.06 T also agrees with the value of 34.80 T obtained by Sorescu *et al*. [99] from their CEMS measurements on $Fe_{50}Co_{50}$ thin film system.

CHAPTER 5

CONCLUSIONS AND RECOMMENDATIONS

5.1 Conclusions

The effect of 20% Fe in the sintered WC-10Co-20Fe sample has been investigated in this work. The hardness value of 1160 ± 42 HV was obtained for the as-sintered WC-10Co sample which decreased to 776 ± 35 HV for the as-sintered WC-10Co-20Fe sample an effect of incorporating additional binder volume of Fe (20%). The addition of 20% Fe increases the hardness value of the sample however the high volume of the binder contents (10% Co and 20% Fe) results in a lower hardness value. The microstructural analysis of the as-sintered samples WC-10Co and WC-10Co-20Fe samples confirm the presence of the starting powders used and also indicate the presence of elemental impurities which might have originated from the starting powders used or the production process. The XRD analysis shows no significant difference between the as-milled powder and as-sintered samples as the XRD patterns confirm the presence of WC and Co in both samples. However, a striking difference was observed between the as-milled powder and as-sintered samples of WC-10Co-20Fe. XRD analysis confirms the presence of WC and Co phases in the as-milled powder and WC and CoFe indicating a phase transformation in the sample. Rietveld analysis was used to detect the fractional change in the *d*-spacing by obtaining the strain ratio. The strain value obtained for the as-sintered WC-10Co sample gives a value of 3.62×10^{-7} for the WC strain ratio and a Co strain ratio of 7.07×10^{-4}. The strain values obtained for the as-sintered WC-10Co-20Fe sample are 2.18×10^{-7} for the WC strain ratio and 1.28×10^{-3} for the CoFe strain ratio.

The presence of iron in the as-milled sample was confirmed by Mössbauer spectroscopy and XRD. The existence of only α-Fe reveals that in the milling of the starting powders of WC, Co and Fe there was no phase transformation. Since there was no phase transformation, this observation was in accordance with the XRD analysis results for the as-milled powder (Figure 4.11) where only the starting powders were identified. This is in good agreement with the work performed by

Bafubiandi's work [100] where no phase change occurs during the milling of WC, Co and hematite. However, there could be possibilities of others elements reacting during the milling process not detectable by Mössbauer spectroscopy. The CEMS measurement on the sintered WC-10Co-20Fe sample shows the formation of new Co-Fe phases as a result of reaction occurring during the sintering process.

5.2 Recommendations

In conclusion, to the best of our knowledge this dissertation has reported the first Mössbauer results on the as-sintered WC-10Co-20Fe sample. However, to gain a better understanding of this sample, the following complementary measurements are suggested for further studies:

- Neutron diffraction measurements need to be conducted to support the XRD analysis from which the relative strain results were obtained.
- For the as-milled powder sample (WC-10Co), further work should be performed focusing on stress analysis of the cobalt phase while for the as-sintered sample, future efforts should be focused on stress analysis of the cobalt iron phase.
- The incorporation of dilute Fe (~10^{-4} at %) in the sintered WC-10Co sample using ^{*57}Mn on-line emission Mössbauer measurements would be beneficial to track the secondary Fe ions and to determine respective hyperfine parameters and any Fe phase formations.
- Theoretical modelling of Fe species in the as-milled and as-sintered WC-10Co samples using Quantum Espresso to determine the lattice location of Fe in the samples under study and compare with experimental results. The envisaged approximations used within this programme include the local spin-density approximation (LSDA) and generalized gradient approximations (GGA).

APPENDICES

Appendix A: Rietveld Analysis

The Rietveld refinement program is a technique used to detect a relatively small strain in a sample [61]. It is powerful techniques used to extract structural details from powder diffraction data. The Rietveld system minimizes the weighted calculation of squared differences between the computed and observed intensity by utilizing the model function. The minimized function, Φ [101] is expressed as:

$$\Phi = \sum_{i=1}^{n} W_i \left(Y_i^{obs} - Y_i^{cal} \right)^2 \quad \text{(A.1)}$$

where, W_i is the weight labelled to the i^{th} data point and the summation is conducted on all the measured data points, n. For Rietveld analysis, the following numerical factors are normally used. The profile residual factor, R_p [102]:

$$R_p = \sum_{i=1}^{n} \frac{\left(Y_i^{obs} - Y_i^{cal} \right)}{\sum_{i=1}^{n} Y_i^{obs}} \times 100 \quad \text{(A.2)}$$

The weighted profile residual, R_{wp}:

$$R_{wp} = \left[\frac{\sum_{i=1}^{n} W_i \left\{ Y_i^{obs} - Y_i^{cal} \right\}}{\sum_{i=1}^{n} W_i (Y_i^{obs})^2} \right]^{1/2} \times 100 \quad \text{(A.3)}$$

The expected profile residual, R_{exp}:

$$R_{\exp} = \left[\frac{n - p}{\sum_{i=1}^{n} W_i (Y_i^{obs})^2} \right]^2 \times 100 \quad \text{(A.4)}$$

where p denote the number of free least squares parameters. The goodness of fit, χ^2 [102] :

$$\chi^2 = \frac{\sum_{i=1}^{n} W_i \left\{ Y_i^{obs} - Y_i^{cal} \right\}}{n-p} = \left[\frac{R_{wp}}{R_{\exp}} \right]^2 \qquad \text{(A.5)}$$

χ^2 should be minimum for best fitted data.

Appendix B: Fitting using Vinda

The Mössbauer data for the as-milled powder WC-10Co-20Fe and the as-sintered WC-10Co-20Fe samples were analyzed using the spreadsheet based tool Vinda developed by H. P. Gunnlaugsson [75]. The procedures for the fitting process and error calculations are described below.

B.1 Introduction to Vinda

Vinda is a set of routines to facilitate the use of Microsoft Excel to analyse Mössbauer data. It is an Add-In for Microsoft Excel which used all the built-in features of MS-Excel for the analysis and presentation of data. Some of the essential features of Vinda are:

- There are no constrains on the types of models.
- Simultaneous analysis of data is possible through the Excel sheet.
- Vinda has the ability to preserve models.
- It has easy access to plotting tools, function evaluation and other features in the spreadsheet program.

B.2 Reading a spectrum in Vinda

A spectrum is read according to the file format which requires that the file format be changed before it can be read. Figure B1 depicts a typical Vinda tool bar for spectral analysis. The calibration menu is used for performing the calibration process. The calibration of a Mössbauer spectrum is carried out by finding the transformation that takes the x-axis in channels and transforms it into a velocity scale with the spectrum of a reference α-Fe foil. The calibration involves folding of the spectrum, since the spectrum is recorded twice, as the source approaches the sample and when the source moves away from the sample.

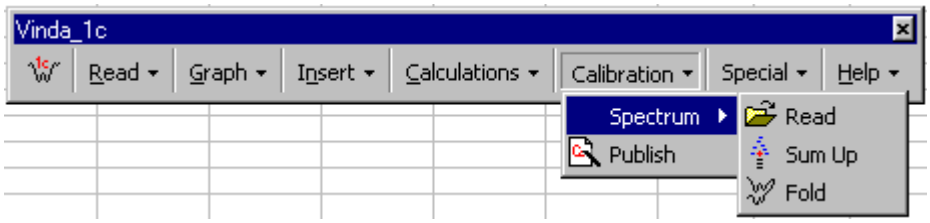

Figure B1: The calibration menu.

To read the spectra into Vinda, the following steps are taken;

- Read the spectra in as illustrated in the calibration menu.
- Sum up. If the spectrum is recorded in 1024 points, then 256 points are used in the analysis.
- Find the folding offset and folding. This is done by optimizing the chi-square value at the top of the sheet by varying the folding offset. After finding the folding offset, the spectrum is then folded and the calibration spectrum is displayed on the graph window with the simulation as shown by Figures B2 and B3. On the right of the sheet, the meaning of the parameters for the chi-square value can be seen graphically.

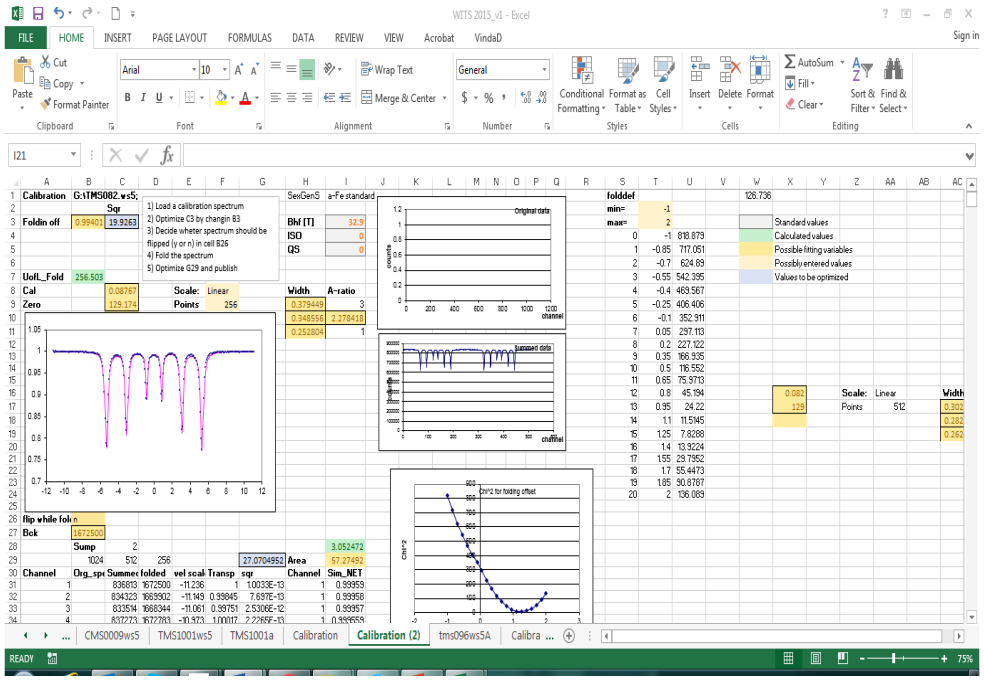

Figure B2: A typical calibration sheet for a TMS spectrum for the *α*-Fe foil used in this study.

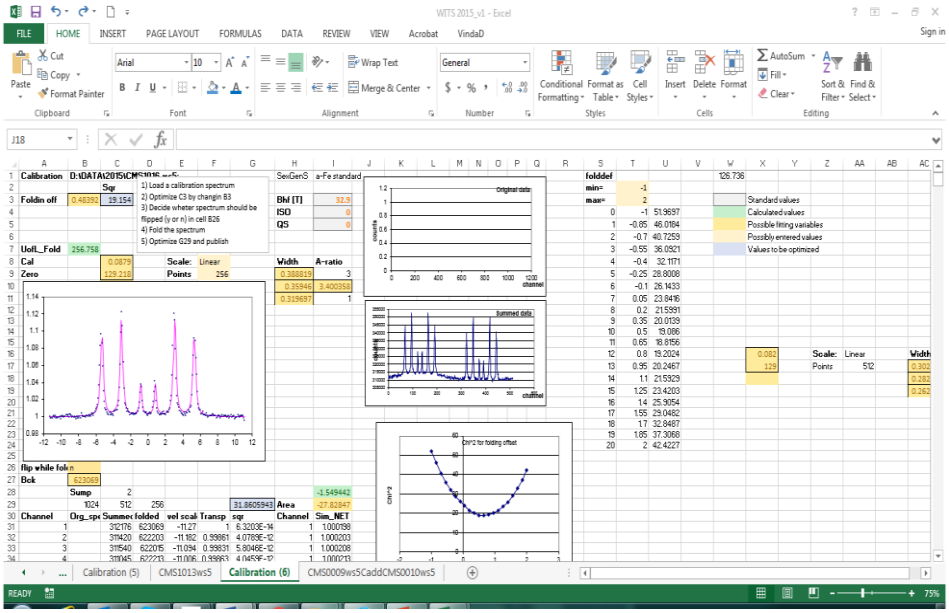

Figure B3: A typical calibration sheet for a CEM spectrum for the *α*-Fe foil used in this study.

B.3 Single Spectrum fitting

Fitting of the spectrum is performed firstly by varying the fitting parameters to obtain a desirable fit and inputting the spectral components together with their corresponding models. The fitting process is done by selecting the chi-square cell (F30) which is the target cell and minimizing it with selected parameters (background, hyperfine parameters, line-widths and areas) with the aid of the solver parameter dialog box. Figure B4 shows the dialog box for the solver parameters.

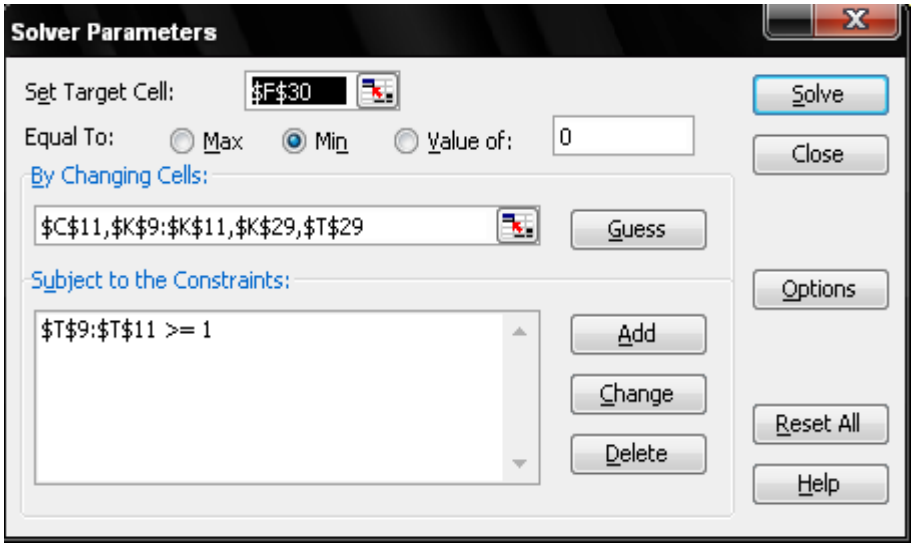

Figure B4: Solver parameter dialog box.

An example of a typical spreadsheet for a single spectrum fitting from the solving process is illustrated in Figure B5 and B6.

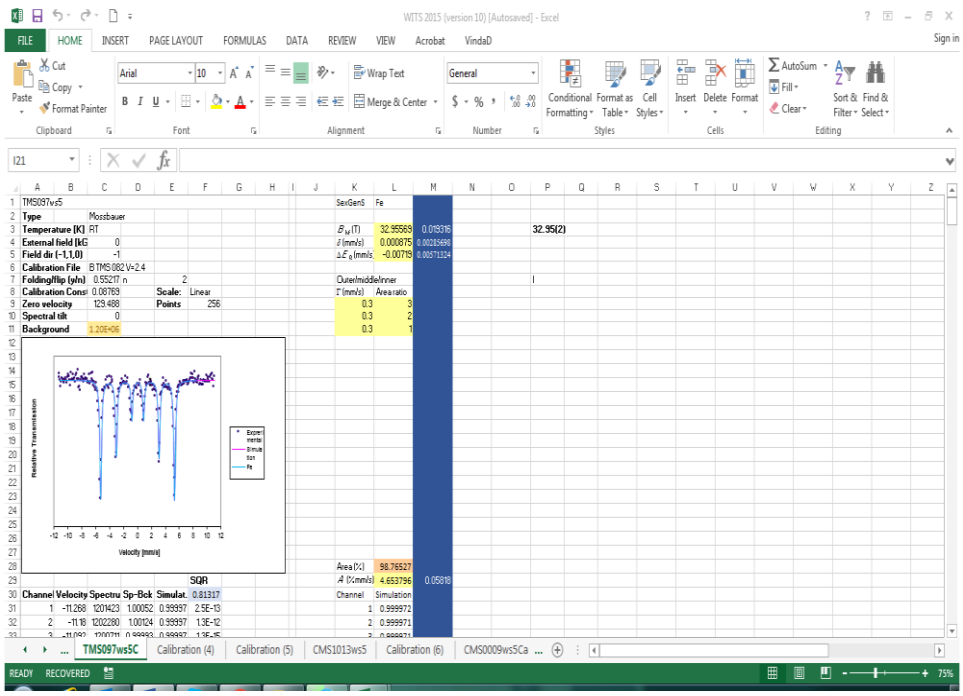

Figure B5: Spreadsheet with fitting parameters obtained from the TMS measurement for the milled WC-10Co-20Fe sample.

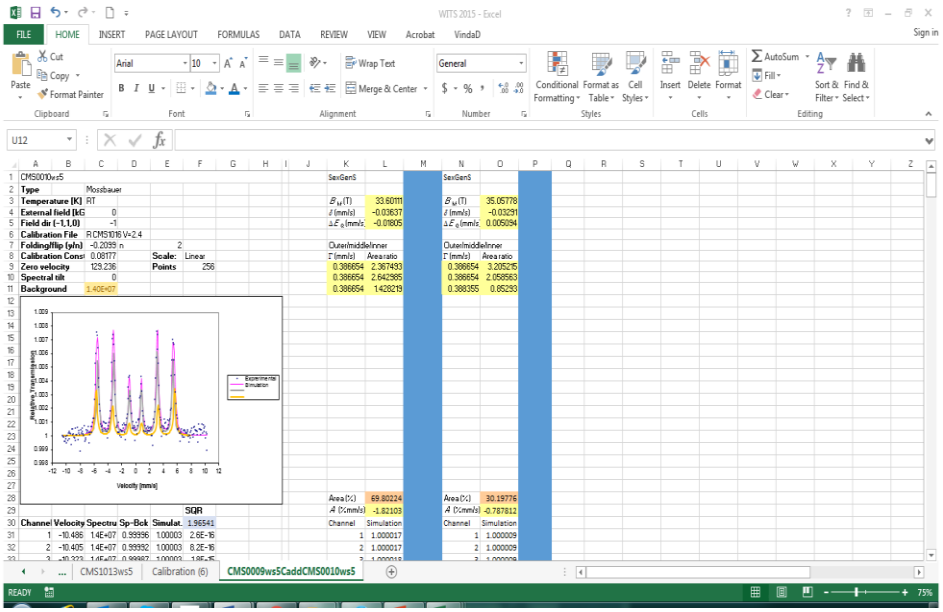

Figure B6: Spreadsheet with fitting parameters obtained from the CEMS measurement for the as-sintered WC-10Co-20Fe sample.

B.4 Error analysis

The calculated errors are determined from the chi-squared value χ^2 which is defined by the equation:

$$\chi^2 = \sum_{i=1}^{N} \frac{\left(Data_i - Simulation_i\right)^2}{Data_i}$$

The chi-square value (F30) in Figure B6 is normalized by the number of data points which is perfect fit as $\chi^2 = 1$. Hence, the number of points should be supplied to the error analysis dialog box as depicted in Figure B7. For more accurate results, the number of iterations should greater than 1.

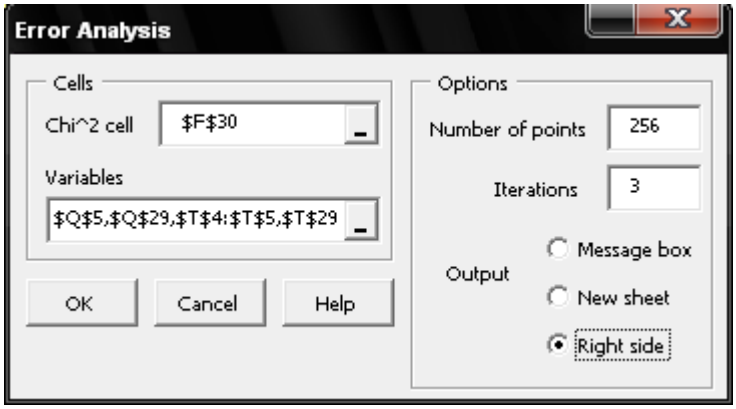

Figure B7: Error Analysis dialog box.

REFERENCES

[1] F.L Zhang, C.Y. Wang and M. Zhu, "Nanostructured WC/Co Composite Powder Prepared by High energy ball milling," *Scripta Materialia*, vol. 49, pp. 1123-1128, 2003.

[2] T.J. Davies and T. Farooq, "Tungsten Carbide hardmetals cemented with Ferroalloys," *Int. Journal Powder Metallurgy*, vol. 27, pp. 347, 1991.

[3] B.J. Marques, C.M. Fernandes and A.M.R. Senos, "Sintering Microstructure and Properties of WC-AISI304 Powder Composites," *Journal Alloy Compound*, vol. 562, pp. 164-170, 2013.

[4] T.W. Penrice, "Alternate binders for hard metals," *Carbide Tool J.*, vol. 20, no. 4, pp. 12-5, 1988.

[5] W. Schedler, "Hard Metals for Practical Users," *VDI-Verlag,Dusseldorf*, Vols. 5-29, 1988.

[6] G. Schneider, "Principles of Tungsten Carbide Engineering," *Society of Carbide and Tool Engineers*, 1989.

[7] H.C. Kim, H.K. Park, I.K. Jeong, I.Y. Ko and I.J. Shon, "Sintering of binderless WC- MO2C hard materials by rapid sintering process," *Ceramics International*, vol. 34, no. 6, pp. 1419-1423, 2008.

[8] G.R. Anstis, P. Chantikul, B.R. Lawn and D.B. Marshall, "A critical evaluation of indentation techniques for measuring fracture toughness," *Journal of the American Ceramics Society*, vol. 64, no. 9, pp. 533-538, 1981.

[9] J.H. Han and D.Y. Kim, "Determination of three -dimensional grain size distribution by linear intercept measurement," *Acta Materialia*, vol. 46, no. 6, pp. 2021-2028, 1998.

[10] Z. Yao, J. Stiglich and T.S Sudarshan, "Nano-grained Tungsten Carbide Cobalt (WC/Co)".

[11] H.E. Exner, ""Physical and Chemical Nature of Cemented Carbides"," *Int. Metal Rev*, vol. 4, pp. 149, 1979.

[12] J. Gurland, "Microstructural Aspects of the Strength and Hardness of Cemented Tungsten Carbides in Materials Metal Cutting," UK.

[13] K. Mannesson, I. Borgh and A. Borgenstam "Abnormal grain growth in Cemented Carbides-Experiments and Simulations," *Int. Journal of Refractory Metals and Hard Materials*, vol. 29, pp. 488-494, 2011.

[14] C.C. Koch, *Material Science Forum*, vol. 243, pp. 88-90, 1992.

[15] G. Rixecker, *Physical Statistic Solid*, vol. 305, pp. A173, 1999.

[16] G. Rixecker, *Hyperfine Interactions*, vol. 130, pp. 127, 2000.

[17] G. Rixecker, "The difficulty of isolating grain boundary components in the Mössbauer spectra of ball-milled materials: iron and silver-iron allys," *Solid State communications*, vol. 122, pp. 299-302, 2002.

[18] G.S. Collins and P. Sinha, *Hyperfine Interactions*, vol. 949, pp. 92, 1994.

[19] In-Jin Shon, In-Kyoon Jeong, In-Yong, Jung-Mann Doh and Kee-Do Woo, "Sintering behaviour and mechanical properties of WC-10Co,WC-10Ni and WC-10Fe hard materials," *Elsevier, Ceramics International*, vol. 35, pp. 339-344, 2009.

[20] H.C. Kim and D.Y. Oh. and I.J. Shon, "Sintering of nanophase WC-15Vol%Co hard metal by rapid sintering process," *Elsevier, Int. Journal of Refractory Metals and Hard materials*, vol. 22, pp. 197-203, 2004.

[21] V. Martins, W. Rodriques and P. Ferrandini, "Comparative Studies of WC-Co and WC-Co-Ni Composites obtained by Conventional Powder Metallurgy," *Materials Research Rev.*, vol. 14, 03, June 2011.

[22] D. Kim, Y. Choi and S. Jung, "Characteristic of Nanophase WC and WC-3wt% Alloy Using a Rapid Sintering Process for Applicationof Friction Stir Processing Tool," in *Advances in Materials Science and Engineering*, Republic of Korea, Hindawi Publishing Corporation, 2014.

[23] M. Mahmoodan, R. Gholamipour and H. Aliakbarzadeh, "Microsturctural and mechanical characterization of high energy ball milled and sintered WC-10wt%Co-xTaC Nano Powders," *Elsevier, Int. Journal of Refractory Metals and Hard Materials*, vol. 27, pp. 801-805, 2009.

[24] A.D. Krawitz and D.L. Coats, "Effect of particle size on the thermal residual stress in WC-Co Composites," *Elsevier, Materials and Engineering*, vol. A359, pp. 338-342, 2003.

[25] J. Gurland, "Temperature and Stresses in the two phase alloy WC-Co," *Trans. America Society Metals*, vol. 50, pp. 1063-71, 1958.

[26] S. Öhman, S. Palmguist and E. Pärnama, "Studies of residual stresses in WC-Co Systems," *Jernkotorets Ann*, vol. 151, pp. 126-59, 1967.

[27] DN. French, "X-ray Stress Analysis of WC-Co Cerments," *J. Amer. Ceram. Society*, vol. 52, pp. 267-75, 1969.

[28] V. Livescu, B. Clausen, J.W. Pagget and M. Bourke, "Measurement and Modelling of room temperature Co-deformation in WC-10wt%Co.," *Material Science Engineering,* vol. A2005;399, pp. 134-40.

[29] C.T. Liu and J. Gurland, *Trans. Am. Scoiety Metal,* vol. 58, pp. 66-73, 1965.

[30] E.J. Lavernia and S. Ho, *Application Composite Material,* vol. 2, pp. 1-30, 1995.

[31] A.D. Krawitz and S. Majundar, *Material Science Engineering,* vol. A123, pp. L1-L3, 1990.

[32] A.D. Krawitz, D.G. Reichel and R.L. Hitterman, *Material Science Engineering,* vol. A119, pp. 127-134, 1989.

[33] D. Mari, A.D. Krawitz, J.W. Richardson and W. Benoit, *Material Science Engineering,* vol. A209, pp. 197-205, 1996.

[34] J. Willbrand, "Archiv Fur das Eisenhuttenwesen," vol. 43, pp. 503-508, 1972.

[35] E.A. Almond and B. Roebuck, *International Material Rev.,* vol. 33, pp. 90-110, 1988.

[36] J.B.J.W. Hegeman, "Grinding of WC-Co Hardmetals," *Elsevier,* 24,Nov. 2000.

[37] M.D. Dyar, D.G. Agresti, M.W. Schaefer, E.C. Sklute and C.A. Grant, ""Mössbauer Spectroscopy of Earth and Planetary Materials"," *Annual Rev. of Planet Science,* 2006.

[38] C. Chen and Y. Qiu, "Mössbauer Spectroscopy," *Royal Society of Chemistry,* 2010.

[39] Department of Physics, Technical Univ. of Munich, " The Discovery of Mössbauer Effect," *Hyperfine Interactions,* vol. 126, pp. 1-12, 2000.

[40] D.L. Williamson, L. Niesen and G. Weyer , *Elsevier,* 1992.

[41] T.C. Gibb and N.N. Greenwood, " Mössbauer Spectroscopy", London: Chapman and Hall Ltd, 1971.

[42] D. Yang and Y. Chen, Mössbauer Effect in Lattice Dynamics: Experimental Techniques and Applications, Germany: Wiley-VCH, 2007.

[43] C. Chen and Y. Qiu, "Nuclear Analytical Techniques for Metallonics and Metalloproteonics," in *Mössbauer Spectroscopy,* 2010.

[44] E. Kuzmaan, Z. Homonnary, S. Nagy, E. Lorand and K. Nomura, Handbook on Nuclear Chemistry, Springer, 2011.

[45] F.J. Berry and D.P.E. Dickson, Mössbauer Spectroscopy, UK: Cambridge University Press, 1986.

[46] E. Bill, P. Gütlich, Mössbauer Spectroscopy and Transition Metal Chemistry: Fundamentals and Applications, Springer, 1978.

[47] E. Kuzmaan, A. Vertes and S. Nagy, "Critical Review of Analytical Apllications of Mössbauer Spectroscopy illustrated by Mineralogical and Geological Examples".

[48] D.H. Ryan and J.M. Cadogan, Mössbauer Spectroscopy Handbook of Applied Solid State Spectro..

[49] H. Masenda, Are Fe and Co implanted ZnO and III-Nitride Semiconductors Magnetic? Phd Thesis, Univ. of the Witwatersrand, 2014.

[50] B.D. Cullity, Elements of X-ray Diffraction, Addison-Wesley Inc., 1978.

[51] D. Louër and J.I. Langford, "Powder Dffraction," *Rep. Prog. Phys.*, vol. 59, pp. 131-234, 1996.

[52] J.E. Post and D.L. Bish, Modern Powder Diffraction, P.H. Ribbe, Ed., Virginia,USA, 1989.

[53] R.M. German, P. Suri and S.J. Park "Review: Liquid phase Sintering," *J. Mater. Science,* vol. 44, pp. 1-39, 2009.

[54] K.J.A. Brookes, "Hardmetal and other Hard Materials International Carbide Data," *Hertfordshire,* 1975.

[55] G.E. Sandland and R.L. Smith, "An Accurate Method of determining the hardness of Metals,with Particular Reference to those of a High Degree of Hardness," 1922.

[56] G.E. Dieter, "Mechanical Metallurgy," pp. ISBN 0-07-100406-8, 1988.

[57] M. Mathew, K.S. Raviashankar and K. Shenoy, "Vickers Hardness and Specific wear resistance of E glass reinforced Poly methyl methacrylate," *Int. Journal of Scientific and Engineering Research,* vol. 5, no. 6, pp. ISSN 2229-5518, June 2014.

[58] U. Täffner, U. Schäfer and V. Carle, "Preparation and Microstructural Analysis of High Performance Ceramics," *ASM International*, vol. 9, 2004.

[59] E. Lloyd, "Atomic number and crystallographic constrast images with the SEM: a review of backscattered electron techniques," 1987.

[60] J.I. Goldstein and E. Newbury Scannning Electron Microscopy and X-ray Analysis, New York: Springer, 2003.

[61] D. Balzar, N. Audebrand, M.R. Daymond, A. Fitch, A. Hewat, J.I. Langford, A. Bail, O. Masson, C.N. McCowan, N.C. Popa, P.W. Stephens and B.H. Toby, "Size-strain line broadening analysis of the ceria round-robin sample.," *Journal of Applied Crystallography,* vol. 37, pp. 911-924, 2004.

[62] Alexander and H. L.E., X-ray Diffraction Procedures for Polycrystalline and Amorphous Materials, New York: Wiley, 1974.

[63] J.R. Gancedo, M. Gracia and J.F. Macro, *Hyperfine Interactions,* vol. 83, pp. 71-78, 1994.

[64] "Data Acquistion Module CMCA-550 Instruction Manual," Wissenschaftliche Elektronik Gmbh, Germany, 2004.

[65] "Application of Conversion Electron Mössbauer Spectroscopy to the study of single crystal specimen", *Surface Science,* vol. 52, pp. 549-552, 1975.

[66] Z.W. Bonchev, A. Jordanov and A. Minkova "Nucl. Instru. Meth.," vol. 70, no. 36, 1969.

[67] K.R Swanson and J.J. Spijkerman, *J. Applied Physics,* vol. 41, pp. 3155, 1970.

[68] J.J. Spijkerman, Mössbauer Effect Methodology, I.J. Gruverman, Ed., New York: Plenum, 1971.

[69] M. Gracia and J.R. Gancedo, *Hyperfine Interact.,* vol. 28, p. 1097, 1986.

[70] L. Sbriz, G. Valconi and M. Villagran, *J. Radioanalytical Nucl. Chem.,* vol. 128, pp. 387, 1988.

[71] M. Villagran, G. Valconi and L. Sbriz, "J. Radioanalytical Nucl. Chem.," vol. 153, p. 375, 1991.

[72] M. Gracia and L. Sbriz, *J. Radiaoanalytical Nucl. Chem.,* vol. 133, p. 211, 1989.

[73] K. Nomura, Y. Ujihira and A. Vertes "Applications of Conversion Electron Mössbauer Spect. (CEMS)," *J. Radioanal. and Nucl. Chem.,* vol. 202,

no. 1-2, pp. 103-199, 1996.

[74] J.R. Gancedo, M. Gracia and J.F Marco "CEMS Methodology," *Hyperfine Interact.,* vol. 66, pp. 83, 1991.

[75] H.P. Gunnlaugsson, "Vinda User Manual".

[76] B. Roebuck, M.Gee and E. G. Morrel, Mechanical test for Hardmetals, United Kingdom: National Physical Laboratory, 1999.

[77] H. Kim, In-Jin Shoon, Jin- Kook Yoon and Jung-Mann Doh, "Consolidation of ultra fine WC and WC-Co hard materials by pulsed current activated sintering and its mechanical properties," *Refractory metals and hard materials,* vol. 25, pp. 46-52, 2007.

[78] H. Singh, "Ph.D Thesis; Synthesis and Characterization of Nano Tunsgten Carbides from ores.," School of Physics and Materials Science, Thapar University, Patiala, 2013.

[79] S.G. Shin, "Experimental and simulation studies on grain growth in TiC and WC-based cermets during liquid phase sintering," *Met. Mater. Int.,* vol. 6, pp. 195-201, 2000.

[80] M.J. Ledoux, C.H. Pham, J. Guille and H. Dunlop, "Compared activities of platinum and high specific surface area MO2C and WC catalysts for reforming reactions.," *J. Catal,* vol. 134, pp. 383-398, 1992.

[81] L. Prakash, Development of tungsten carbide hard metals using iron-based binder alloys, Ph.D Thesis Institute for Material and Solid State Research, Kernforschungszentrum, 1980.

[82] R. Lima, J. Karthikeyan, C. Kay, J. Lindemann and C. Berndt, "Microstructural characteristics of cold-sprayed nanostructured WC-Co coatings," *Elsevier, Thin Solid Films,* vol. 416, pp. 129-135, 2002.

[83] G. Lee and S. Kang, "Sintering of nano-sized WC-Co powders produced by a gas reduction-carburization process.," *Elsevier, J. of Alloys and Compounds,* vol. 419, pp. 281-289, 2006.

[84] J. Sun, F. Zhang and J. Shen, "Characterizations of ball-milled nanocrystalline WC-Co composite powders and subsequently rapid hot pressing sintered cermets," *Elsevier, Materials Letters,* vol. 57, pp. 3140-3148, 2003.

[85] S. Amberg and H. Doxner, "Porosity in cemented carbides," *Powder Metallurgy,* vol. 20, no. 1, pp. 1-10, 1977.

[86] K. Niihara, R. Morena and D. Hasslman, "Evaluation of KIC of brittle solids by the indentation method with low crack-to-indent ratio," *Journal of Materials Science Letters,* vol. 1, pp. 13-16, 1982.

[87] C. Suryanarayana, "Mechanical alloying and milling," *Prog. Mater. Science,* vol. 46, pp. 1-84, 2001.

[88] S. Hewitt and K. Kibble, "Effects of ball milling time on the synthesis and consolidation of nanostructured WC-Co composites," *Elsevier,* vol. 27, pp. 937-948, 2009.

[89] C. Wei, X. Song, S. Zhao, L. Zhang and W. Liu, "In-situ synthesis of WC-Co composite powder and densification by sinter-HIP," *Elsevier, Inter. Journal of Refractory Metals and Hard Materials,* vol. 28, pp. 567-571, 2010.

[90] M. Eskandarany, A. Mahday, H. Ahmed and A. Amer, "Synthesis and Characterizations of ball milled nanocrystalline WC and nanocomposite WC-Co powders and subsequent consolidations," *Elsevier, J. of Alloys and compound,* vol. 312, pp. 315-325, 2000.

[91] H.M. Rietveld, *J. Appl. Cryst,* vol. 2, pp. 65-71.

[92] In. Shon, In. Jeong, In. Ko, J. Doh and K. Woo, "Sintering behaviour and mechanical properties of WC-10Co,WC-10Ni and WC-10Fe hard materials produced by high-frequency induction heated sintering," *Elsevier, Cereamics International,* vol. 35, pp. 339-344, 2009.

[93] HG. Jiang, H. Hm and E.J. Lavernia, "Synthesis of Fe-rich Fe-Al nanocrystalline solid solutions using ball milling," *J. Mater Res,* vol. 14, pp. 1760-70, 1999.

[94] H. Zhang, "The Mössbauer spectra of carbon-coated iron and iron compound nanocrystals produced by arc discharge," *Journal of Material Science Letters,* vol. 18, pp. 919-920, 1999.

[95] E. Jartych, M. Jalochowski and M. Budzynski, "Influence of the electrodeposition paramters on surface morphology and local magnetic properties of thin iron layers.," *Elsevier, Applied Surface Science,* vol. 193, pp. 210-216, 2002.

[96] H. Zhang, "The Mössbauer spectra of graphite-encapsulated iron and iron compounds nanocrystals prepared in carbon arc method.," *Elsevier, Journal of Physics and Chem. of Solids,* vol. 60, pp. 1845-1847, 1999.

[97] G. Alcazar, L. Zamora, J. Marco, J. Romero, J. Gonzalez and F. Palomares, "Magnetic and structural characterisation of mechanically Alloyed $Fe_{50}Co_{50}$ sample," *Universidad del Valle,* pp. 41-47, 2011.

[98] G. Collins and B. Meeves, "Formation of FeCo mechanical Alloying," *Scripta Metall. and Mat.,* vol. 29, pp. 1319-1323, 1993.

[99] M. Sorescu and A. Grabias, "Structural and Magnetic properties of $Fe_{50}Co_{50}$ System," *Elsevier, Intermetallics,* vol. 10, pp. 317-321, 2002.

[100] A. Bafubiandi, "Mössbauer Spectroscopy study of mechanically alloyed Fe_2O_3," *Hyperfine Interactions,* vol. 168, pp. 1017-1022, 2006.

[101] B. Toby, "R factors in Rietveld analysis: How good is good enough?," *Powder Diffraction,* vol. 21, 2006.

[102] R. Young, "Introduction to the Rietveld method," in *The Rietveld Method*, Oxford, Oxford University Press, 1993, pp. 1-38.